Neuron

Article

TDP-43 seeding induces cytoplasmic aggregation heterogeneity and nuclear loss of function of TDP-43

Graphical abstract

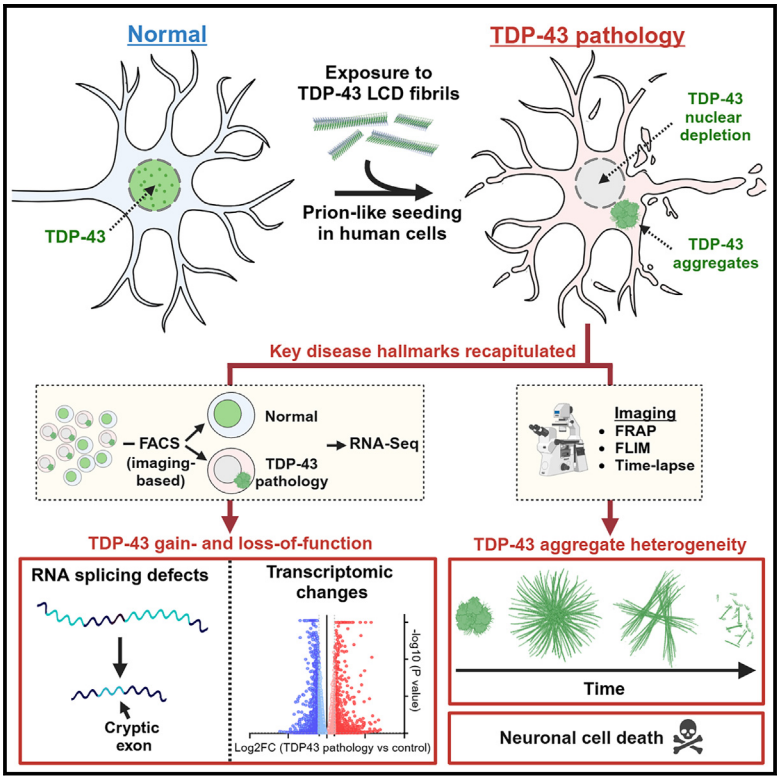

Highlights

- Amyloid-like fibrils trigger TDP-43 cytoplasmic aggregation and nuclear loss of function
- Seeded TDP-43 aggregates recapitulate key disease hallmarks in human neurons
- TDP-43 pathology yields a unique transcriptomic signature and splicing defects
- Progressive degradation of TDP-43 aggregates induces pathological heterogeneity

Authors

Jens Rummens, Bilal Khalil, Günseli Yıldırım, ..., Frederic Rousseau, Joost Schymkowitz, Sandrine Da Cruz

Correspondence

sandrine.dacruz@kuleuven.be

In brief

Rummens et al. demonstrate that amyloid-like fibrils trigger TDP-43 aggregation and nuclear depletion, key hallmarks of neurodegenerative disorders. This provokes a unique transcriptomic signature with RNA splicing defects, including disease-specific cryptic splicing in human cells. Over time, fibril-induced TDP-43 pathology recapitulates distinct aggregate shapes and causes toxicity in iPSC-derived neurons.

Rummens et al., 2025, Neuron *113*, 1597–1613
May 21, 2025
https://doi.org/10.1016/j.neuron.2025.03.004

CellPress

Neuron

CellPress
OPEN ACCESS

Article

TDP-43 seeding induces cytoplasmic aggregation heterogeneity and nuclear loss of function of TDP-43

Jens Rummens,[1] Bilal Khalil,[1] Günseli Yıldırım,[1,2] Pedro Silva,[3] Valentina Zorzini,[2,4] Nicolas Peredo,[5] Marta Wojno,[6] Meine Ramakers,[2] Ludo Van Den Bosch,[7] Philip Van Damme,[8,9] Kristofer Davie,[10] Jelle Hendrix,[3] Frederic Rousseau,[2] Joost Schymkowitz,[2] and Sandrine Da Cruz[1,11,*]

[1]Laboratory of Neurophysiology in Neurodegenerative Disorders, VIB-KU Leuven Center for Brain & Disease Research, Department of Neurosciences, KU Leuven, Leuven Brain Institute, 3000 Leuven, Belgium
[2]Switch Laboratory, VIB-KU Leuven Center for Brain & Disease Research, Department of Cellular and Molecular Medicine, KU Leuven, 3000 Leuven, Belgium
[3]Dynamic Bioimaging Lab, Advanced Optical Microscopy Centre and Biomedical Research Institute (BIOMED), Hasselt University, 3590 Diepenbeek, Belgium
[4]Biophysics Expertise Unit, VIB-KU Leuven Center for Brain & Disease Research, 3000 Leuven, Belgium
[5]VIB Bio-Imaging Core, VIB-KU Leuven Center for Brain & Disease Research, 3000 Leuven, Belgium
[6]VIB Single Cell & Microfluidics Unit, VIB-KU Leuven Center for Brain & Disease Research, 3000 Leuven, Belgium
[7]Laboratory of Neurobiology, VIB-KU Leuven Center for Brain & Disease Research, Department of Neurosciences, KU Leuven, 3000 Leuven, Belgium
[8]Laboratory of Neurobiology, Department of Neurosciences, KU Leuven, 3000 Leuven, Belgium
[9]Neurology Department, University Hospitals Leuven, 3000 Leuven, Belgium
[10]VIB Single Cell Bioinformatics Expertise Unit, VIB-KU Leuven Center for Brain & Disease Research, 3000 Leuven, Belgium
[11]Lead contact
*Correspondence: sandrine.dacruz@kuleuven.be
https://doi.org/10.1016/j.neuron.2025.03.004

SUMMARY

Cytoplasmic aggregation and nuclear depletion of TAR DNA-binding protein 43 (TDP-43) are hallmarks of several neurodegenerative disorders. Yet, recapitulating both features in cellular systems has been challenging. Here, we produced amyloid-like fibrils from recombinant TDP-43 low-complexity domain and demonstrate that sonicated fibrils trigger TDP-43 pathology in human cells, including induced pluripotent stem cell (iPSC)-derived neurons. Fibril-induced cytoplasmic TDP-43 inclusions acquire distinct biophysical properties, recapitulate pathological hallmarks such as phosphorylation, ubiquitin, and p62 accumulation, and recruit nuclear endogenous TDP-43, leading to its loss of function. A transcriptomic signature linked to both aggregation and nuclear loss of TDP-43, including disease-specific cryptic splicing, is identified. Cytoplasmic TDP-43 aggregates exhibit time-dependent heterogeneous morphologies as observed in patients—including compacted, filamentous, or fragmented—which involve upregulation/recruitment of protein clearance pathways. Ultimately, cell-specific progressive toxicity is provoked by seeded TDP-43 pathology in human neurons. These findings identify TDP-43-templated aggregation as a key mechanism driving both cytoplasmic gain of function and nuclear loss of function, offering a valuable approach to identify modifiers of sporadic TDP-43 proteinopathies.

INTRODUCTION

Cytoplasmic aggregation and nuclear clearance of TAR DNA-binding protein 43 (TDP-43) are key pathological hallmarks of several age-related neurodegenerative conditions.[1,2] Cytoplasmic inclusions of TDP-43 accumulate in neurons and glia of ~97% of amyotrophic lateral sclerosis (ALS) and ~45% of frontotemporal dementia (FTD) cases,[3] as well as a number of other neurodegenerative diseases such as Alzheimer's disease (AD) and limbic-predominant age-related TDP-43 encephalopathy (LATE).[4,5]

TDP-43 is a predominantly nuclear RNA-binding protein that plays fundamental roles in RNA metabolism, including transcription, splicing, RNA transport, and translation.[6–10] TDP-43 harbors a C-terminal low-complexity domain (LCD) that facilitates its de-mixing through liquid-liquid phase separation (LLPS).[11–20] Recent findings suggest that TDP-43 LLPS fine-tunes its binding to RNA targets, regulating its normal functions

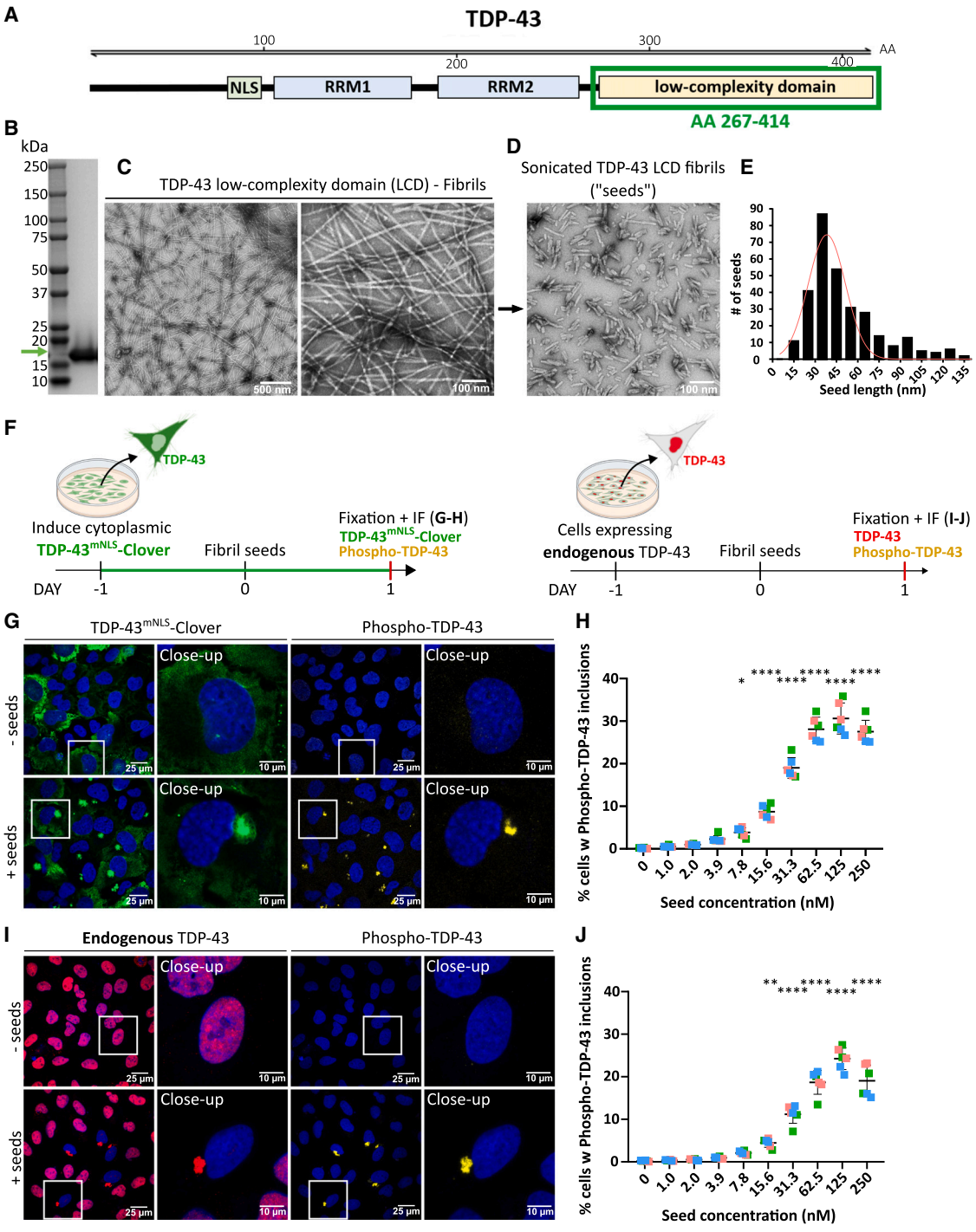

Figure 1. Fibril-induced cytoplasmic aggregation of TDP-43 in human cells

(A) Schematics of TDP-43 structure. NLS, nuclear localization signal; RRM, RNA recognition motif; LCD, low-complexity domain.

(B) Coomassie-stained SDS-PAGE of purified recombinant TDP-43 LCD (amino acid [aa] 267–414).

(C) Electron micrographs of TDP-43 LCD fibrils. Scale bar overview: 500 nm; close up: 100 nm.

(D) Electron micrograph of sonicated TDP-43 LCD fibrils. Scale bar: 100 nm.

(E) Distribution of fibril seed length (nm) (300 seeds from 3 batches). Red curve: Gaussian fit.

(F) Experimental outline to model TDP-43 pathology in U2OS cells expressing TDP-43^{mNLS}-Clover upon doxycycline induction (left) or naive U2OS cells (right).

(G) Immunostaining of TDP-43^{mNLS}-Clover (green), phospho-TDP-43 (yellow), and DAPI (blue) in TDP-43^{mNLS}-Clover cells 1 day post-seed exposure (50 nM). Scale bar overview: 25 µm; close up: 10 µm.

(legend continued on next page)

in RNA processing.[13,21] On the other hand, TDP-43 LCD is highly aggregation-prone,[22–24] and phase-separated droplets have been proposed to act as reaction centers for the formation of pathological aggregates.[11,25–27]

In the central nervous system (CNS) of ALS and FTD patients, TDP-43 is depleted from the nucleus and accumulates in the cytoplasm where it forms detergent-insoluble, ubiquitinated, and hyperphosphorylated inclusions.[1,28] Hence, both TDP-43 loss of function in the nucleus and gain of toxicity in the cytoplasm are thought to drive disease pathogenesis. Interestingly, post-mortem studies reveal extensive heterogeneity in morphology, subcellular localization, and composition of TDP-43 inclusions,[29–31] whereby pathology progresses in a stereotypical manner from the site of initiation to anatomically connected brain regions.[32,33] Accumulation of insoluble TDP-43 was recently reported in cells[34–39] and transgenic mouse models[38,39] through exposure to patient brain extracts, suggesting that pathology in TDP-43 proteinopathies propagates in a self-templating and prion-like fashion.

Despite recent progress, the molecular mechanisms that drive TDP-43 pathology remain poorly understood. This is in part due to the paucity of systems that reliably recapitulate both nuclear depletion and cytoplasmic aggregation of TDP-43. In this study, we exploit the concept of templated aggregation to establish cellular models mimicking key features of human TDP-43 proteinopathies.

RESULTS

TDP-43 LCD assembles into amyloid-like fibrils that seed aggregation in a cell-free assay

To recapitulate templated aggregation of TDP-43 and elucidate the underlying mechanisms, we purified the aggregation-prone TDP-43 LCD as a recombinant protein from overexpression in *E. coli* (Figures 1A and 1B). With time and shaking, TDP-43 LCD spontaneously assembled into fibrillar aggregates, as confirmed by transmission electron microscopy (TEM) (Figure 1C). TDP-43 LCD fibrils form long and unbranched filaments with a mean width of 16 ± 3 nm. The majority (75%) of the filaments possess a helical twist with a mean periodicity of 71 ± 11 nm (Figures S1A–S1D). Thin films of the end-stage aggregates were positively stained with Congo red, as observed under bright-field illumination, and showed green birefringence under polarized light that is typical of amyloid deposits (Figure S1E). Fourier-transform infrared (FTIR) spectroscopy further revealed a main peak in the amide I region at 1,625 cm^{-1}, which is typical of amyloids, and a secondary peak around 1,660 cm^{-1}, which is usually assigned to beta turns (Figure S1F). In addition, these assemblies bound to the amyloid-sensor dye thioflavin-T (ThT) as evidenced by the strong time-dependent increase in fluorescence intensity (Figure S1G). The aggregation kinetics showed a lag phase (31 ± 2 h at 24 μM of monomeric TDP-43 LCD), followed by a rapid growth phase and plateau, typical for amyloid formation. Sonication of the amyloid fibrils resulted in the generation of small fibril fragments with a mean length of 38 ± 13 nm, hereafter referred to as "seeds" (Figures 1D and 1E). Finally, we investigated whether these fragmented fibrils could seed aggregation of monomeric TDP-43 LCD in a molar ratio of 1:20 (monomeric units). Exposure to fragmented fibrils did indeed accelerate aggregation of TDP-43 LCD, effectively removing the lag phase (Figure S1H). The end-stage ThT fluorescence intensity upon seeding correlated with the concentration of monomer. This demonstrates that recombinant fibrils of TDP-43 LCD seed amyloid aggregation in a cell-free environment as previously reported.[17,27]

Fibril-induced cytoplasmic aggregation of TDP-43 in human cells

To test whether recombinant TDP-43 LCD fibrils seed aggregation of cytoplasmic TDP-43 in cultured cells, sonicated fibril fragments (seeds) were introduced by liposome-based transfection into human cells that ectopically express cytoplasmic TDP-43 (Figure 1F, left). We used a genetically engineered U2OS cell line that expresses fluorescently tagged TDP-43 with a disrupted nuclear localization signal (TDP-43^{mNLS}-Clover) in a doxycycline-inducible manner[11] (Figures S2A and S2B). In normal conditions, TDP-43^{mNLS}-Clover displays a diffuse distribution—predominantly in the cytoplasm—as well as reversible condensates via LLPS.[11,40] However, 1 day after seed exposure, fibril-treated cells accumulated TDP-43^{mNLS}-Clover aggregates (Figure 1G). Interestingly, these inclusions were immunopositive for the phosphorylated form of TDP-43 at serine 409/410 (phospho-TDP-43) (Figure 1G), a key feature of pathological inclusions found in ALS/FTD patients. Quantification of cells with phosphorylated TDP-43 inclusions—as well as the size of these inclusions—in response to different seed concentrations revealed a dose-dependent effect (Figures 1H and S2C–S2F), with up to 31% ± 3.7% of the cells accumulating phosphorylated TDP-43^{mNLS}-Clover aggregates.

To further determine whether recombinant TDP-43 LCD fibrils can also seed endogenous nuclear TDP-43 in absence of overexpression of cytoplasmic TDP-43, we exposed naive human U2OS cells to the seeds using the same paradigm (Figure 1F, right). Interestingly, 1-day seed exposure led to cytoplasmic inclusions of endogenous TDP-43 that were phospho-TDP-43 immunopositive, while no inclusions were observed in naive cells that were not exposed to seeds as revealed by immunostaining (Figure 1I). The number and size of these phosphorylated TDP-43 inclusions correlated with seed concentration, with up to 23% ± 2.6% of cells harboring cytoplasmic phospho-TDP-43

(H) Percentage of cells with phospho-TDP-43 inclusions upon dose response of seeds in TDP-43^{mNLS}-Clover cells (related to G). Data point colors indicate 3 experiments. Mean ± SD. Dunnett's one-way ANOVA (*$p < 0.05$; ****$p < 0.0001$).

(I) Immunostaining of endogenous TDP-43 (red), phospho-TDP-43 (yellow), and DAPI (blue) in naive U2OS cells 1 day post-seed exposure (100 nM). Scale bar overview: 25 μm; close up: 10 μm.

(J) Percentage of naive cells with phospho-TDP-43 inclusions upon seed dose response (related to I). Data point colors indicate 3 experiments. Mean ± SD. Dunnett's one-way ANOVA (**$p < 0.01$; ****$p < 0.0001$).

See also Figures S1–S3.

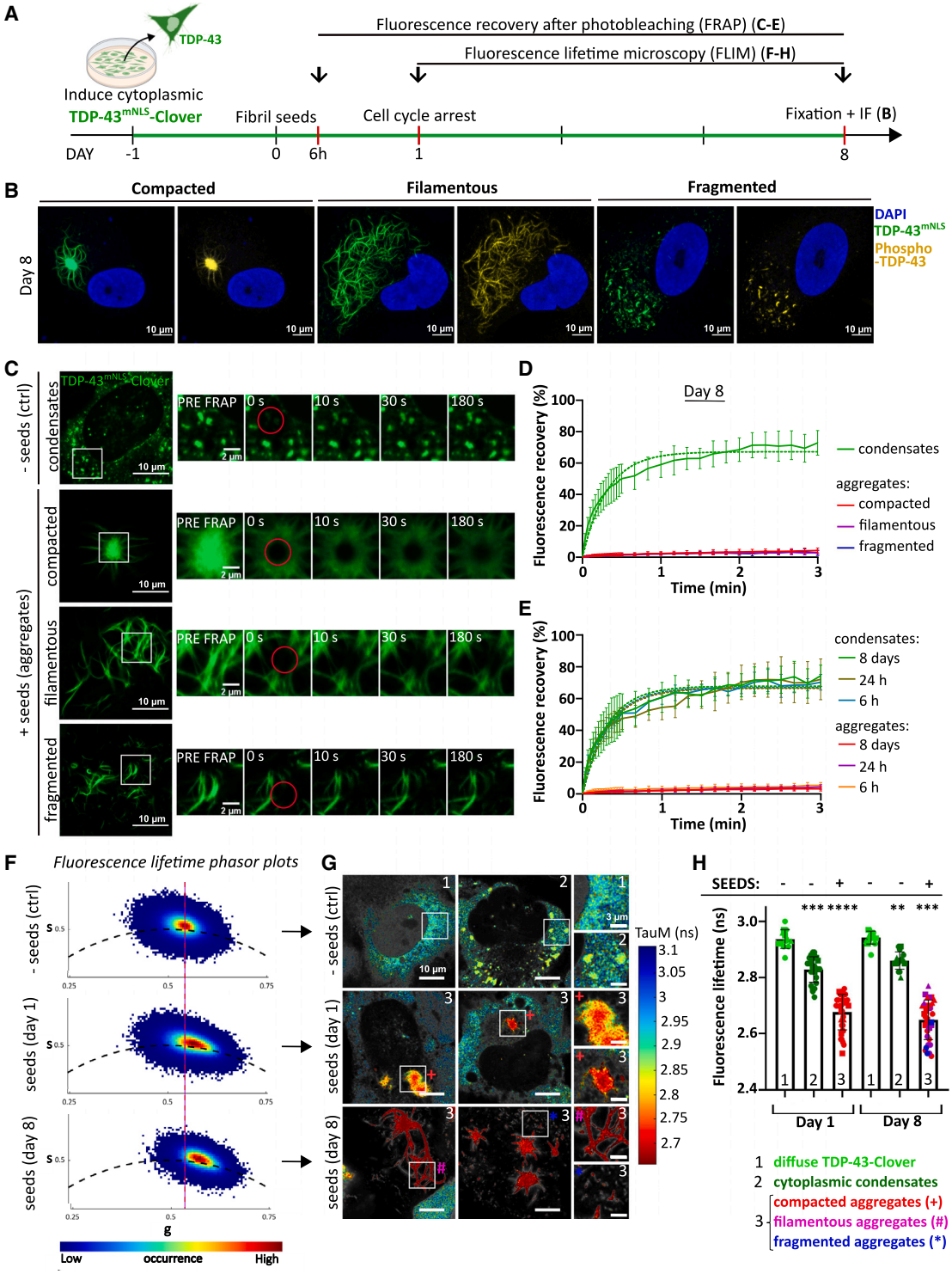

Figure 2. Fibrils induce TDP-43 aggregates with distinct morphologies and biophysical properties

(A) Experimental outline of non-dividing TDP-43^{mNLS}-Clover cells exposed to 50 nM seeds and followed with time by FRAP and FLIM analyses.

(B) Immunostaining of TDP-43^{mNLS}-Clover (green), phospho-TDP-43 (yellow), and DAPI (blue) with compacted/filamentous/fragmented morphologies after 8 days. Scale bar: 10 µm.

(C) FRAP on liquid condensates or seed-induced aggregates of TDP-43^{mNLS}-Clover (green). Red circle: laser-stimulated area. Scale bar overview: 10 µm; close up: 2 µm.

(legend continued on next page)

inclusions (Figures 1J and S2G–S2I). Hence, these data demonstrate that recombinant TDP-43 LCD fibril seeds also induce templated aggregation of endogenous TDP-43 in cells where TDP-43 is predominantly nuclear and that increased accumulation of cytoplasmic TDP-43 prior to fibril exposure is not required to seed endogenous wild-type TDP-43. Yet, a modest decrease in seeding efficiency was observed in naive versus TDP-43^{mNLS}-Clover cells (23% versus 31% at 125 nM seeds), suggesting that mislocalization/increased levels of TDP-43^{mNLS} in the cytoplasm might render the protein more susceptible to seeded aggregation. Interestingly, recombinant TDP-43 LCD fibrils specifically seed aggregation of TDP-43, but not other ALS-linked RNA-binding proteins (FUS and hnRNPA2/B1) whose nuclear localization and expression pattern were not altered by the seeds (Figures S3A and S3B).

Given that the fibrils are histidine (His) tagged, we further immunostained the seeded cells with a poly-His antibody and found that recombinant His-tagged TDP-43 LCD seeds were detected inside TDP-43^{mNLS}-Clover aggregates at 24 h post-seed exposure, but this was lost with time (Figure S3C). It is worth noting that the anti-His antibody staining reveals cross-reactivity with endogenous nuclear proteins, as previously reported,[41] further preventing evaluating the potential presence of His-TDP-43-LCD fibril seeds within the nucleus.

Overall, these data demonstrate that recombinant TDP-43 LCD fibrils specifically induce cytoplasmic hyperphosphorylated TDP-43 aggregates in human cells in a dose-dependent manner, thus supporting a prion-like model wherein TDP-43 aggregation occurs in a templated fashion.

Fibrils induce TDP-43 aggregates with distinct morphologies and biophysical properties

Fibril-induced aggregation in TDP-43^{mNLS}-Clover-expressing cells was initiated shortly after seed exposure (the first aggregates appearing within 2–3 h) and the number of cells with detectable TDP-43 inclusions increased steadily throughout the first day, after which it reached a plateau, as demonstrated by time-lapse fluorescence microscopy (Figure S3D). To investigate TDP-43 aggregation in non-dividing cells in a time-dependent manner, we further assessed how seeded inclusions evolve for a period of 8 days upon continuous expression of cytoplasmic TDP-43 and cell proliferation inhibition (Figure 2A). Prolonged aggregation resulted in a drastic increase in the size of aggregates that frequently occupied the entire volume of the cytoplasm (Figure 2B). Importantly, a range of different aggregate morphologies was produced with time. Three types could be distinguished: "compacted aggregates" that contain a dense core in the center, "filamentous aggregates" that present as a meshwork of filaments without a clear core, and "fragmented aggregates" that consist of small individual fragments (Figure 2B). It is important to note that this is a general classification, and there is still significant heterogeneity within each class.

We subsequently assessed the dynamic properties of the different types of TDP-43^{mNLS}-Clover aggregates using fluorescence recovery after photobleaching (FRAP). As previously reported,[40] in control condition, TDP-43^{mNLS}-Clover forms spherical condensates/droplets in the cytosol, which have liquid properties, as revealed by the fast recovery of the Clover fluorescence upon photobleaching (half-time [$t_{1/2}$] of 13 s) (Figures 2C and 2D). In contrast, the three types of "aged" seeded-TDP-43^{mNLS}-Clover inclusions were solid-like as no fluorescence recovery was observed upon photobleaching of the compacted, filamentous, or fragmented aggregates (Figures 2C and 2D). To assess whether dynamics of fibril-induced TDP-43^{mNLS}-Clover inclusions evolved over time, FRAP measurements were performed at 6 h, 24 h, and 8 days after seed exposure. Early-formed TDP-43 inclusions that were present at 24 or even 6 h after seeding also showed negligible recovery after photobleaching, similar to aged aggregates (Figure 2E), suggesting that they rapidly display solid-like properties.

To determine if the dynamic properties of fibril-induced aggregates of wild-type TDP-43 are similar to those containing TDP-43^{mNLS}-Clover, we co-transfected TDP-43^{WT}-Clover with the recombinant TDP-43 LCD seeds in naive U2OS cells (Figure S4A). In control conditions, TDP-43^{WT}-Clover is predominantly present in the nucleus. However, in the presence of the seeds, TDP-43^{WT}-Clover formed cytoplasmic inclusions that were hyperphosphorylated within 24 h (Figures S4B and S4C). FRAP measurements demonstrated that while nuclear condensates in control cells displayed liquid-like properties (recovery of 72% with $t_{1/2}$ = 15.5 s), fibril-induced cytoplasmic TDP-43^{WT}-Clover inclusions were solid-like (Figures S4D and S4E), similar to TDP-43^{mNLS}-Clover inclusions (Figures 2C–2E).

The fluorescence lifetime of fluorophores can probe for changes in the microenvironment of a protein.[42] To investigate specific properties of Clover-tagged TDP-43 in fibril-induced cytoplasmic aggregates, such as their density/crowding, we performed fluorescence lifetime imaging microscopy (FLIM) on TDP-43^{mNLS}-Clover-expressing U2OS cells in control conditions or at 1 or 8 days post-fibril exposure (Figures 2F–2H). We applied

(D) Mean fluorescence intensity at the bleached area over time for different types of aggregates/condensates at 8 days. Nonlinear regression curve fitted to FRAP data from condensates (dotted line). At least 10 aggregates/condensates per condition from 3 experiments. Mean ± SD.
(E) Mean fluorescence intensity at the bleached area over time for aggregates/condensates at 6 h, 1 day, and 8 days. Nonlinear regression curves fitted to FRAP data from condensates (dotted lines). At least 10 aggregates/condensates per condition from 3 experiments. Mean ± SD.
(F) Phasor plots representing fluorescence lifetime distributions for each condition (no seeds, 1 and 8 days after seeds). Based on at least 25 images per condition from 3 experiments. Vertical dotted line (red) indicates photon-weighted center of mass of the phasor plot in control conditions (no seeds).
(G) Pseudo-colored lifetime images of control cells and cells at 1 or 8 days post-seed exposure. Colors represent Clover lifetime (see color scale). Numbers indicate TDP-43-Clover condensation state (1: diffuse; 2: droplets, 3: aggregates). Symbols indicate aggregate shapes (+, compacted; #, filamentous; *, fragmented). Scale bar overview: 10 μm; close ups: 3 μm.
(H) Mean fluorescence lifetime (TauM at photon-weighted center of mass of the corresponding phasor plot) of TDP-43^{mNLS}-Clover in either (1) diffuse state (no seeds), (2) condensates (no seeds), or (3) aggregates (+ seeds), at 1 or 8 days post-seed exposure. Data points are individual cells from 3 experiments (different shapes represent separate experiments). Mean ± SD. Dunnett's one-way ANOVA (**$p < 0.01$, ***$p < 0.001$, ****$p < 0.0001$).
See also Figure S4.

the phasor analysis approach to FLIM to visualize the complex nature of TDP-43 aggregation, whereby each count in the phasor histogram provides lifetime information corresponding to one pixel in the image.[43,44] When all lifetime data for each of the experimental conditions were combined in a single phasor plot, an overall shift in the fluorescence lifetime could be detected upon fibril seeding, reflecting the appearance of a new TDP-43-Clover species with a shorter lifetime (Figure 2F). In control conditions, we observed that the fluorescence lifetime of TDP-43^{mNLS}-Clover was significantly reduced in cytoplasmic TDP-43 droplets, compared with diffuse pools, confirming that this represents a more "condensed" TDP-43 state (Figures 2G and 2H). Importantly, when TDP-43^{mNLS}-Clover accumulated in aggregates upon fibril exposure at 1 or 8 days after seed exposure, its fluorescence lifetime was further decreased (10% reduction compared with diffuse TDP-43^{mNLS}-Clover), regardless of aggregate morphology (Figures 2G and 2H). Likewise, FLIM analysis of TDP-43^{WT}-Clover cells showed similar results, whereby reduced fluorescence lifetimes are associated with soluble-to-liquid and even more so with liquid-to-solid phase transition (Figures S4F–S4H). Hence, FLIM can accurately sense condensation/aggregation state of fluorescently tagged TDP-43 in cells, and fibril-induced cytoplasmic TDP-43 aggregates have biophysical properties that are distinct from soluble TDP-43.

Fibril-induced nuclear depletion and loss of function of TDP-43 in human cells

We next assessed whether nuclear TDP-43 depletion is also recapitulated in our cellular models. Nuclear endogenous TDP-43 levels were significantly reduced upon aggregation in seeded cells expressing cytoplasmic TDP-43^{mNLS}-Clover (Figures 3A–3C), as well as in naive cells containing uniquely endogenous TDP-43 inclusions (Figures 3D–3F), as evaluated by immunofluorescence. Nuclear depletion in the engineered model was more pronounced in cells wherein the entire pool of cytoplasmic TDP-43^{mNLS}-Clover was present in the aggregated state ("full aggregation"), compared with cells in which only a proportion of cytoplasmic TDP-43^{mNLS}-Clover aggregated ("partial aggregation") (Figure 3C). Time-lapse fluorescence microscopy further revealed that TDP-43 LCD seeding induced first aggregation of cytoplasmic TDP-43^{mNLS}-Clover, followed by depletion of the TDP-43^{mNLS}-Clover pool from the nucleus (Figure S5A).

TDP-43 is an essential regulator of RNA splicing and during disease nuclear TDP-43 depletion leads to aberrant incorporation of cryptic exons in mRNA transcripts,[45,46] such as the FTD-ALS risk gene *UNC13A*.[47,48] Fibril seed exposure in both naive and TDP-43^{mNLS}-Clover-expressing U2OS cells resulted in cryptic exon inclusion in *UNC13A* within 2 days, as detected by RT-PCR, while these cryptic transcripts were not present in control cells that were not exposed to seeds (Figure 3G). Likewise, cryptic exon inclusion upon seed exposure was specifically detected in the six other known TDP-43 splicing targets that we tested[45]: *HDGFL2*, *GPSM2*, *ATG4B*, *EPB41L4A*, *PFKP*, and *AGRN* (Figure 3G).

In order to elucidate transcriptomic alterations caused by both gain and loss of TDP-43 function, image-based fluorescence-activated cell sorting (FACS) of cells with or without aggregates (based on diffusivity of TDP-43^{mNLS}-Clover signal) was performed (Figures 3H, S5B, and S5C), followed by RNA sequencing (RNA-seq). RNA profiles from cells with and without aggregates displayed highly distinct transcriptomic profiles, as revealed by the principal-component analysis (PCA) (Figure S5D). Differential splice junction analysis of the two sorted cell populations further confirmed RNA splicing changes associated with a loss-of-function signature in the TDP-43^{mNLS}-Clover aggregate-containing cells (Figure 3H). Comparison of our dataset with a previously published list of cryptic exons produced in HeLa cells upon TDP-43 knockdown[45] confirms 33 cryptic splicing junctions that are specifically recapitulated in cells with fibril-induced TDP-43^{mNLS}-Clover aggregates (corresponding to 28/41 cryptic exons previously reported in TDP-43-KD HeLa cells) (Figure 3H; Table S1).

Altogether, these findings demonstrate that exposure to amyloid-like TDP-43 fibrils is sufficient to induce nuclear loss of TDP-43 function along with its aggregation in the cytoplasm, hence recapitulating two major hallmarks of human TDP-43 proteinopathy.

Time-dependent degradation and clearance of fibril-induced TDP-43 aggregates

To elucidate pathways that are dysregulated by TDP-43 aggregation and nuclear depletion, we applied differential gene expression (DEG) analysis to the RNA-seq dataset obtained from cells with and without TDP-43^{mNLS}-Clover aggregates (Figure 3H, left). TDP-43 cytoplasmic aggregation and nuclear depletion in our cell model resulted in widespread transcriptomic changes (6,142 and 6,243 genes were upregulated and downregulated, respectively) (Figures 4A and 4B; Table S2). Among the most significantly upregulated genes is *GPNMB* (Figures 4A and 4B), which was recently also found to be strongly upregulated in postmortem ALS spinal cord[49] and which is increased at the protein level in spinal cord, cerebrospinal fluid (CSF), and serum of ALS patients.[50,51] Interestingly, genes associated with neurodegenerative diseases, but also proteostasis- and metabolism-related genes, were found to be highly upregulated in TDP-43 aggregate-containing cells (Figure S5E). In contrast, transcripts encoding several known TDP-43-binding targets (including *TIMP3*, *USP13*, and *STMN2*[46]) were found to be downregulated in cells with TDP-43 aggregates, further strengthening that fibril treatment not only induces TDP-43 gain of toxicity but also loss of function (Figure 4A).

Cytoplasmic TDP-43 inclusions that accumulate in the CNS of ALS and FTD patients are ubiquitinated[1] and co-localize with the ubiquitin-binding protein p62,[53] which acts as a cargo receptor to shuttle substrates to the autophagosome and proteasome. Interestingly, *SQSTM1*—the gene encoding p62—was found to be highly upregulated ($\log_2$ fold change [l2fc] = 2.6) in cells with fibril-induced TDP-43 aggregates (Figures 4A and 4B). Moreover, we demonstrate that seeded TDP-43^{mNLS} inclusions are positively immunolabeled with antibodies recognizing poly-ubiquitin and p62. Each marker co-localized with 1-day-old TDP-43 inclusions, as well as with more "mature" 8-day-old TDP-43 aggregates (Figure 4D). Of note, p62 could be detected in forming TDP-43 inclusions as soon as 6 h after seed exposure, indicating that this is an early event (Figure S6A). Likewise, fibril-induced

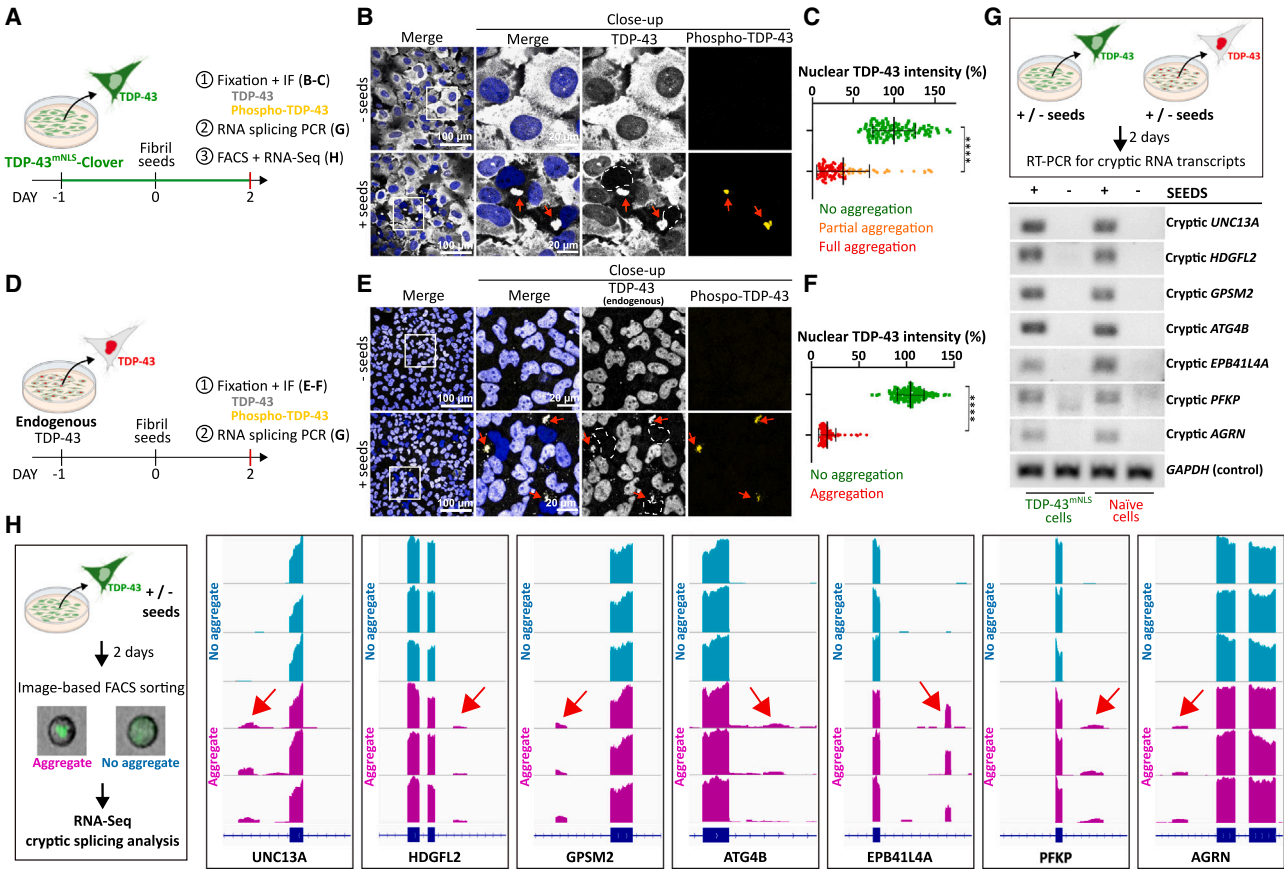

Figure 3. Fibril-induced nuclear depletion and loss of function of TDP-43 in human cells

(A) Experimental outline of TDP-43^{mNLS}-Clover U2OS cells 2 days post-seed exposure (50 nM) and further analyzed by immunostaining, RT-PCR, and RNA-seq.

(B) Immunostaining of total TDP-43 (white), phospho-TDP-43 (yellow), and DAPI (blue) in TDP-43^{mNLS}-Clover U2OS cells. Red arrows indicate TDP-43^{mNLS}-Clover inclusions. Scale bar overview: 100 μm; close up: 20 μm.

(C) Mean nuclear TDP-43 intensity in cells with full (red) and partial (orange) TDP-43^{mNLS}-Clover aggregation or without aggregates (green). Data points are nuclei from 3 experiments. Mean ± SD. Unpaired t test (****$p < 0.0001$).

(D) Experimental outline of naive U2OS cells 2 days post-seed exposure (100 nM) and further analyzed by immunostaining and RT-PCR.

(E) Immunostaining of endogenous TDP-43 (white), phospho-TDP-43 (yellow), and DAPI (blue) in naive U2OS cells. Red arrows indicate TDP-43 inclusions. Scale bar overview: 100 μm; close up: 20 μm.

(F) Mean nuclear TDP-43 intensity in cells with aggregates (red) or without aggregates (green). Data points are nuclei from 3 experiments. Mean ± SD. Unpaired t test (****$p < 0.0001$).

(G) RT-PCR analysis of *de novo* cryptic RNA transcripts in naive or TDP-43^{mNLS}-Clover cells 2 days post-seed (or control buffer) exposure. *GAPDH* transcript was used as control.

(H) TDP-43^{mNLS}-Clover U2OS cells with and without aggregates, respectively, isolated using image-based FACS 2 days post-seed exposure, followed by RNA-seq to identify RNA splicing changes (left). Visualization of cryptic exons located in *UNC13A*, *HDGFL2*, *GPSM2*, *ATG4B*, *EPB41L4A*, *PFKP*, and *AGRN* genes. RNA-seq reads from cells without aggregates (top, blue) or with aggregates (bottom, purple) are aligned to the hg38 genome (reads from 3 experiments). Cryptic exons (red arrows) are specifically detected in cells with aggregates. Gene annotations are shown below in blue, labeling exons (thick) and introns (thin) (right). See also Figure S5 and Table S1.

aggregates of TDP-43^{WT}-Clover were also ubiquitin and p62 positive (Figures S6E and S6F).

Multiple pathways of cellular proteostasis have been proposed to play a role in the degradation of TDP-43 aggregates.[54–57] Over 75% of known proteasomal subunits were found to be upregulated at the transcriptomic level in the seeded cells, along with lysosomal and heat shock proteins (HSPs) (Figure 4C; Tables S3–S5), but also autophagy-related genes were differentially expressed (upregulated or downregulated) upon TDP-43 aggregation (Figure 4C; Table S6). We subsequently assessed the localization of components of the proteostasis machineries (Figures 4E, 4F, and S6). Proteasomal markers PSMA1 and PSMC4—subunits of the core and regulatory proteasome complex, respectively—co-localized with TDP-43^{mNLS}-Clover inclusions (Figures 4E and S6B), and lysosomal LAMP1-positive vesicles strongly accumulated in the proximity of 1- or 8-day-old TDP-43^{mNLS}-Clover aggregates (Figures 4F and S6C). In contrast, EEA1—a marker of early endosomes—did not accumulate around aggregates (Figure S6D). In line with these findings, in seeded naive cells, PSMA1 also co-localized with fibril-induced

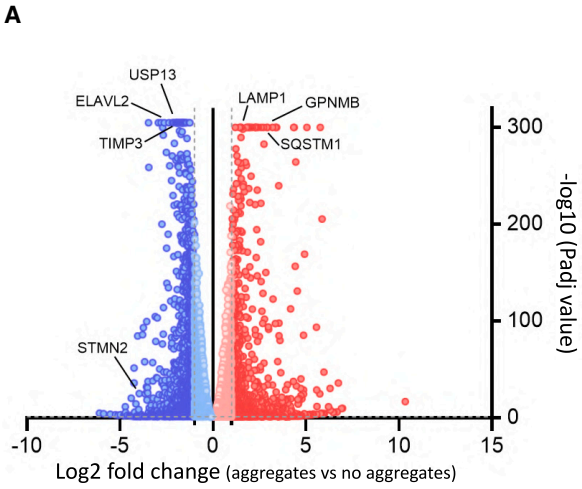

C **Differentially expressed proteostasis genes (DOWN or UP)**

PROTEASOME		LYSOSOME		AUTOPHAGY	HEAT SHOCK
PSMB7	PSMD13	NEU1	ATP6V1G1	SQSTM1	HSPA1B
PSMA1	PSMA6	CLCN7	ATP6V0D1	WIPI1	HSPA1A
PSMD2	PSMB3	TPP1	GAA	MAP1LC3B2	HSPE1
PSMB10	PSMA2	GNS	ATP6V0B	ATG2A	HSPD1
PSMB1	PSMF1	LAMP1	ATP6V1E1	MAP1LC3B	HSPA6
PSMC4	PSMA7	ATP6V1A	CLCN3	GABARAP	HSPBAP1
PSMB8	PSMB9	CTSA	CTSB	OPTN	HSPA8
PSMG4	PSMC2	CTSO	CTSL	ATG3	HSPA9
PSMD3	PSMA4	ATP6V1F	MCOLN1	GABARAPL2	HSPA4
PSMD6	PSMC5	ATP6V1H	ATP6V1D	ULK1	HSP90AB1
PSMG1	PSMD14	CTSD	ATP6V0A2	ATG4D	HSPB2
PSMA3	PSMD16	GLA	ATP6V0E1	ATG10	HSPB8
PSMB5	PSMG3	SCPEP1	ATP6V0C	WIPI2	HSPBP1
PSME4	PSMD8	HEXA	CTSH	ATG4A	HSP90AA1
PSMB6	PSMB2	GBA		ATG4C	HSP90B1
PSMB4	PSMC1	CD63		MAP1LC3C	HSPA13
PSMA5		PSAP			HSPG2
PSMD11		CTSC			HSPB7

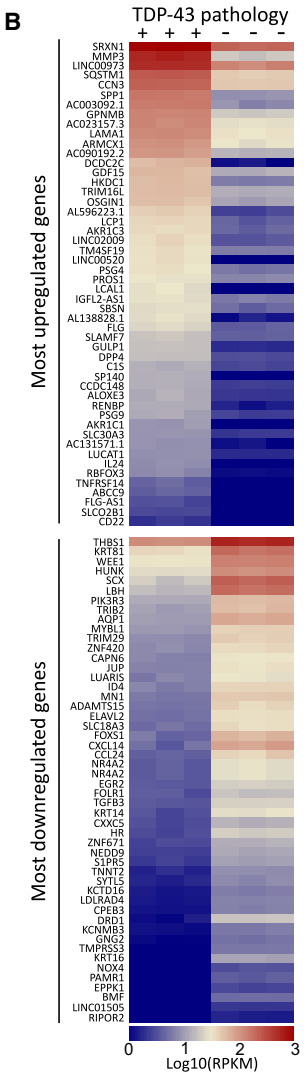

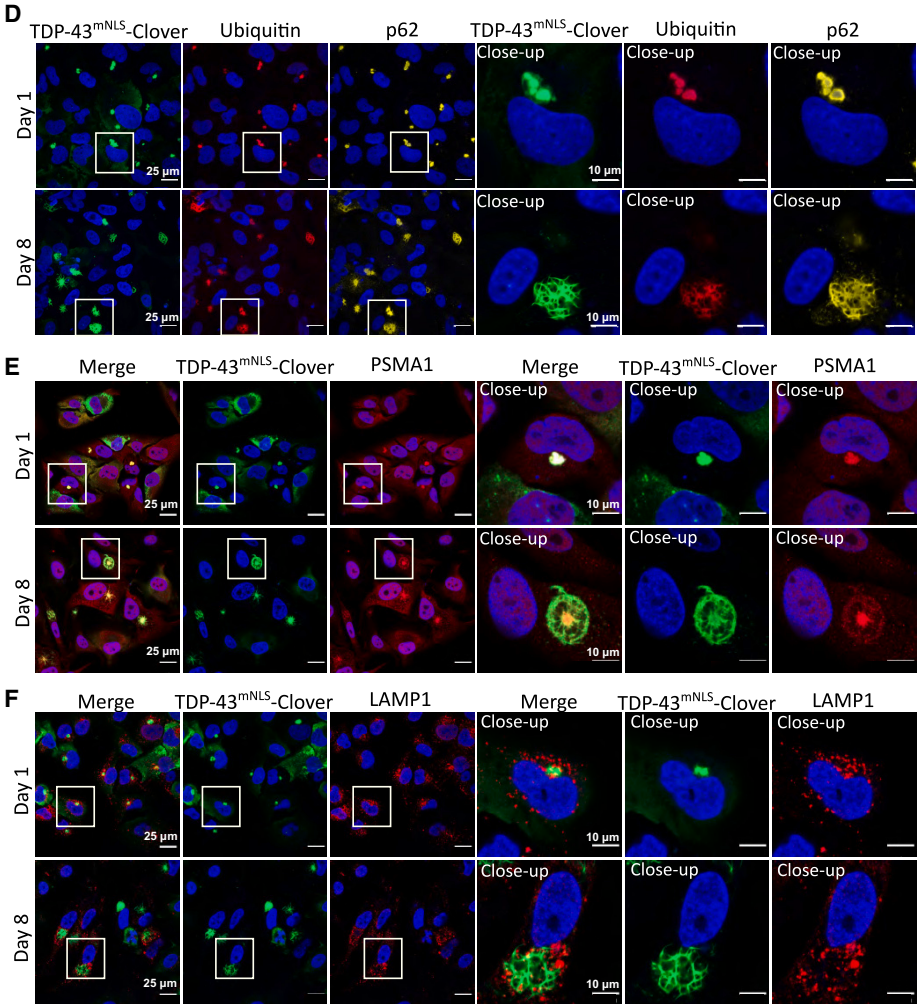

(legend on next page)

TDP-43^{WT}-Clover aggregates (Figure S6G), while the lysosomal re-localization was less evident around the wild-type compared with mutant TDP-43-containing aggregates (Figure S6H). Overall, these findings suggest that fibril-induced aggregation of TDP-43 rapidly results in sustained recruitment of protein degradation machinery.

To directly test whether seeded TDP-43 aggregates undergo degradation with time, we quantified the number of cells harboring TDP-43 aggregates—as well as the morphology of those aggregates—at fixed time points after seeding (Figure 5A). We find that the proportion of distinct morphologies of seeded TDP-43 aggregates changes with time (Figures 5A–5D). While at 2 days post-seeding the compacted shape represents most of the aggregates (97%), by 5 and 8 days only 60% and 39% of the aggregates are compacted, respectively, and have typically acquired a "star-shaped" morphology. Instead, large aggregates consisting of intricate filamentous networks appear at 5 days (31%) along with aggregates with a more fragmented morphology (9%), the latter of which represented 20% of the aggregates by 8 days, suggesting potential active degradation (Figures 5A–5D). Interestingly, treatment of seeded TDP-43^{mNLS}-Clover cells with proteasome inhibitors bortezomib or MG-132 was sufficient to prevent these time-dependent morphological changes in aggregates (Figures S7A and S7B). Indeed, aggregates that were continuously treated with low doses of bortezomib or MG-132 mostly remained small and compacted up to 6 days after seeding. These findings support that different types of aggregates recapitulated in our model represent different degradation stages and suggest that these time-dependent morphological changes are at least partially mediated by the proteasomal machinery.

Despite the obvious transition in morphology of the aggregates over time, no clear reduction in the number of aggregate-containing cells could be detected when constitutive expression of TDP-43^{mNLS}-Clover was maintained (Figure 5C). Therefore, we took advantage of the doxycycline-regulatable expression system to restrict expression of TDP-43^{mNLS}-Clover in time (Figure 5E). When expression was restricted to 2 days, the number of aggregate-containing cells was reduced at day 5 after seeding (reduction by 26%), with a more pronounced decrease at day 8 (reduction by 73%) (Figures 5F and 5G), whereby more than half of the remaining aggregates displayed a fragmented morphology (Figure 5H). A 2-day period of live imaging of TDP-43^{mNLS}-Clover aggregates (starting at 7 days post-seeding) confirmed active degradation of the aggregates into individual filaments, followed by smaller fragments that eventually disappeared (Figure 5I).

Fibril-induced TDP-43 pathology in cultured cell lines is not associated with overt toxicity

As shown in Figure 5C, the percentage of cells that harbor seeded TDP-43 aggregates remains largely unchanged over time—at least in conditions of continuous TDP-43^{mNLS}-Clover expression and cell-cycle inhibition. However, the total number of cells (regardless of whether or not cells were exposed to the seeds) significantly reduced with time (Figures S8A and S8B), suggesting that toxicity in this model is not related to aggregation per se but is likely a consequence of constitutive mutant TDP-43 expression.

To evaluate the impact of TDP-43 aggregation/condensation states on cell viability, individual TDP-43^{mNLS}-Clover-expressing cells were tracked for 2 days using time-lapse fluorescence imaging (Figure S8C). Surprisingly, cell death probability (i.e., percentage of cells undergoing cell death within the 2-day imaging period) was undistinguishable between cells containing fibril-induced aggregates versus those with diffuse TDP-43^{mNLS}-Clover (25%). However, a 2.5-fold increased cell death probability (64%) was observed in cells containing TDP-43^{mNLS}-Clover droplets (Figure S8D). Hence, the presence of cytoplasmic TDP-43-Clover in a condensed state (TDP-43 droplets) is associated with an increased cell death probability, in contrast to cytoplasmic TDP-43 in a diffuse or aggregated state. As a result, these cells cannot be used to study cell death mechanisms induced by TDP-43 aggregation and/or loss of function.

Fibrils induce TDP-43 pathology in human iPSC-derived neurons in a time-dependent fashion

We next tested whether recombinant TDP-43 LCD fibrils also recapitulate TDP-43 pathology in human neuronal cells. For this purpose, we used human induced pluripotent stem cells (iPSCs) with a doxycycline-inducible neurogenin-2 (NGN2) transcription factor cassette that enables their differentiation into cortical-like neurons (i3Neurons).[58] These cells were genetically engineered to stably express, close to endogenous levels, TDP-43^{WT}-Clover (Figures S9A and S9B) and were cultured in doxycycline-containing induction medium for 3 days to allow their differentiation into neuronal precursor cells (NPCs), followed by culturing in neuron medium for further neuronal maturation (Figure 6A). Differentiating neurons showed robust expression of neuronal markers (NeuN, Tau, MAP2) from day 6 post-induction onward (Figure S9C). Importantly, when NPCs were treated with TDP-43 LCD fibril seeds (250 nM, directly added to the medium) for 2 days, this resulted in the accumulation of cytoplasmic, hyperphosphorylated TDP-43^{WT}-Clover inclusions in 5% of neuronal precursors (Figures 6B and 6D), but

Figure 4. Fibril-induced TDP-43 aggregation triggers upregulation and recruitment of proteostasis machinery

(A) Volcano plot of differentially expressed genes in U2OS cells with TDP-43^{mNLS}-Clover aggregates versus U2OS cells with non-aggregated (diffuse) TDP-43^{mNLS}-Clover. Upregulated genes are shown in red and downregulated genes in blue.

(B) Heatmap showing expression levels of most significantly (top 50, based on p adj.) upregulated and downregulated genes with l2fc > 2 or l2fc < −2, respectively, in cells with aggregates (n = 3) or without aggregates (n = 3). Color scale represents $\log_{10}$(RPKM).

(C) List of genes encoding proteasomal, lysosomal, autophagy-related, or heat shock proteins (HSPs) that are differentially expressed in cells with TDP-43-Clover aggregates. Upregulated genes (l2fc > 0.3; p adj. < 0.0001) are shown in red and downregulated genes (l2fc < −0.3; p adj. < 0.0001) in blue. Established gene lists for autophagy activation and lysosomal biogenesis[52] were used as guidelines.

(D–F) Immunostaining of ubiquitin (red) and p62 (yellow) (D), proteasomal marker PSMA1 (red) (E), and lysosomal marker LAMP1 (red) (F) in TDP-43^{mNLS}-Clover (green) U2OS cells at 1 and 8 days post-seed exposure. Scale bar overview: 25 μm; close up: 10 μm.

See also Figure S6 and Tables S2 and S3–S6.

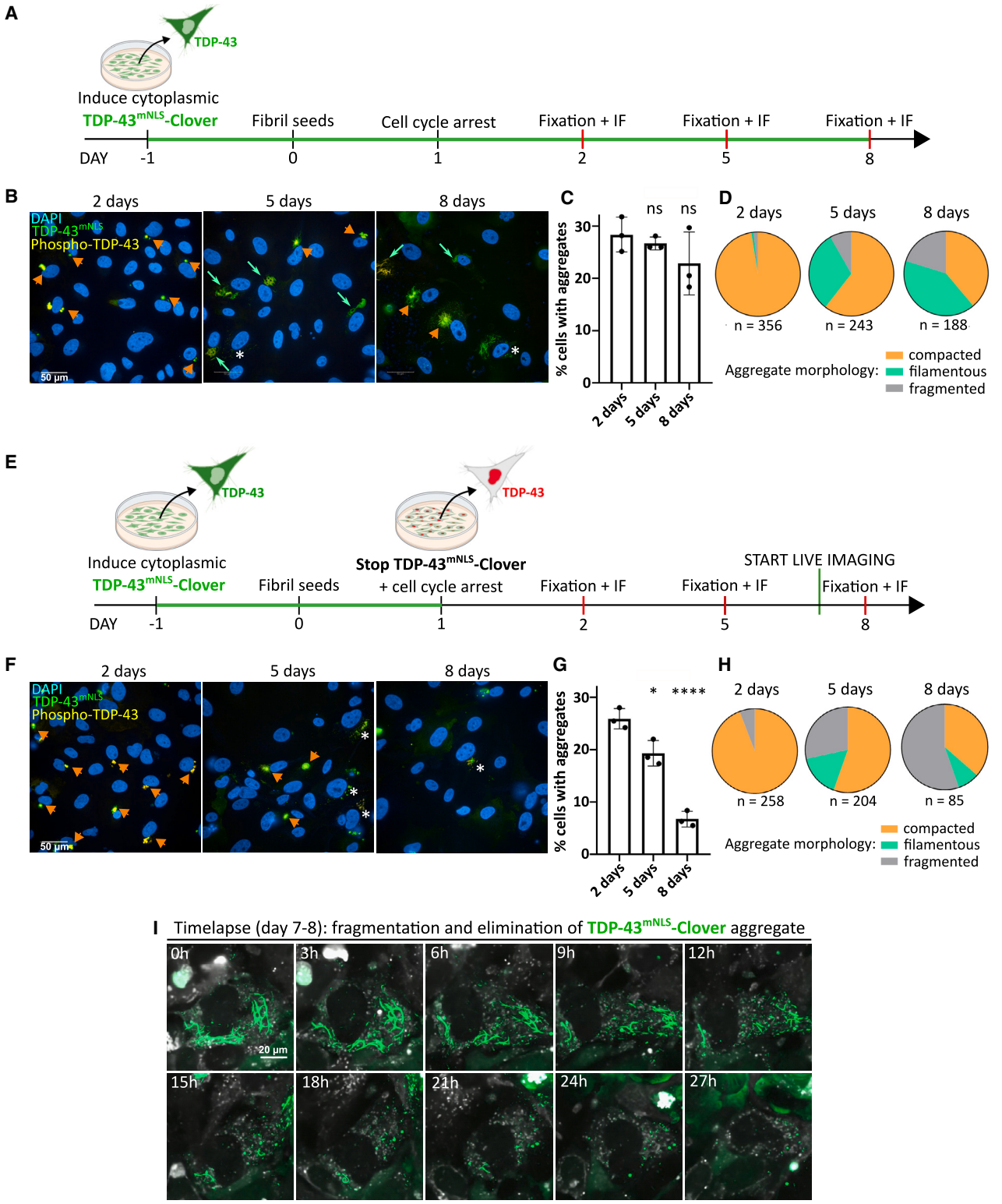

Figure 5. Time-dependent remodeling and clearance of fibril-induced TDP-43 aggregates

(A) Experimental outline of non-diving TDP-43^{mNLS}-Clover cells exposed to 50 nM seeds in the presence of doxycycline for constitutive TDP-43^{mNLS}-Clover expression over time (see B–D).

(legend continued on next page)

also in differentiated neurons at 5 and 7 days post-seed treatment (3.4% and 2.1%, respectively), while aggregation was completely absent from control cells at all time points (Figures 6D and S9D). Fibril-induced TDP-43^{WT}-Clover inclusions showed negligible fluorescence recovery upon photobleaching, as opposed to nuclear condensates in control cells (recovery $t_{1/2}$ = 13.4 s), confirming that TDP-43 within neuronal inclusions is also in an aggregated state as in U2OS cells (Figures S9E and S9F).

Fibril seed treatment also induced TDP-43 nuclear clearance in ~30% and ~50%–55% of the iPSC-derived neurons with TDP-43-Clover aggregates at 2 and 5–7 days post-fibril addition, respectively, as revealed by immunostaining (Figures 6E and S9D) and by time-lapse fluorescence imaging of TDP-43-Clover (Figure 6F). TDP-43 nuclear clearance resulted in cryptic splicing of UNC13A and HDGFL2 mRNAs (Figure 6G), as well as in a reduction of stathmin-2 protein levels (46% decrease compared with control cells) (Figures 6H and 6I), demonstrating that exposure to TDP-43 LCD fibril seeds induces nuclear loss of function of TDP-43 in iPSC-derived neurons.

The overall percentage of neurons with phosphorylated TDP-43 aggregates reduced over time (Figure 6D), which was accompanied by a transition from dense compacted inclusions to fragmented aggregates (Figures 6B and 6C). This could suggest that TDP-43^{WT}-Clover aggregates are gradually degraded. Accordingly, fibril-induced TDP-43^{WT}-Clover aggregates also co-localized with ubiquitin and p62 (Figure S10A), as well as with the proteasomal marker PSMC4 (Figure S10B), but no clear accumulation of LAMP1 in/around TDP-43 aggregates was observed (Figure S10C), consistent with our results in naive U2OS cells transfected with TDP-43^{WT}-Clover (Figure S6H). In contrast to our findings in U2OS cells whereby TDP-43-containing aggregates were well tolerated with no overt toxicity, a time-dependent increased cell death was observed in human neurons containing TDP-43 aggregates, compared with neurons without aggregates (Figure 6J, 31% and 60% of death in cells with aggregates, compared with 13% and 29% in control cells, at 5 and 7 days, respectively), further confirmed by time-lapse fluorescence imaging (Figure S10D). This toxicity is likely to contribute to the time-dependent reduction in the number of neurons with TDP-43 aggregates observed in Figure 6D.

Finally, we tested whether fibril seeds also induce endogenous TDP-43 pathology in human neurons derived from parental, non-engineered naive iPSCs (Figures 6K and S11A–S11D). Consistently with our findings in the engineered neurons, fibril treatment produced cytoplasmic phosphorylated endogenous TDP-43 inclusions in 5% of the cells within 2 days, whereby the percentage of iPSC neurons with fibril-induced TDP-43 aggregates reduced with time (3.0%, 2.9%, and 1.4% at 5, 7, and 10 days, respectively) (Figures S11B and S11C). A time-dependent cell death that is more pronounced in cells with aggregates, compared with cells without aggregates, was observed, suggesting that fibril-induced pathology of endogenous TDP-43 is toxic for human neurons (Figure S11D). Notably, the onset of toxicity occurred later than in TDP-43-Clover neurons, likely due to lower baseline cell death in parental iPSCs, allowing us to monitor pathology up to 10 days post-seed treatment, by which time only 1.4% of neurons had aggregates with a reduced size (Figures S11C and S11D).

Hence, recombinant TDP-43 LCD fibrils induce cytoplasmic aggregation, along with nuclear loss of function of TDP-43, in human iPSC-derived neurons. This pathology is targeted for degradation and associated with neuronal toxicity in a time-dependent fashion.

DISCUSSION

Nuclear depletion and cytoplasmic aggregation of TDP-43 in neurons and glia are key hallmarks of several neurodegenerative diseases.[2,59] We produced amyloid-like fibrils from the aggregation-prone LCD of TDP-43 and demonstrated that fragmented TDP-43 LCD fibrils (seeds) rapidly induce mislocalization of TDP-43 in cytoplasmic inclusions that are ubiquitinated and phosphorylated at serine 409/410. This is consistent with our previous effort[11] whereby fibril exposure in neuron-like cells induced cytoplasmic de-mixing of TDP-43. Importantly, previous studies report that detergent-insoluble autopsied material from patients with TDP-43 proteinopathy induces aggregated and hyperphosphorylated TDP-43 in cells[35–39,60–62] and transgenic mice,[38,39] suggesting that these extracts contain pathogenic material (presumably TDP-43 fibrils) that seeds aggregation of cellular TDP-43. Altogether, these findings strongly support a prion-like paradigm wherein TDP-43 aggregation

(B) Immunostaining of TDP-43^{mNLS}-Clover (green), phospho-TDP-43 (yellow), and DAPI (blue) at 2, 5, and 8 days post-seed exposure. Symbols indicate aggregate shapes (compacted: orange arrowhead; filamentous: green arrow; fragmented: white star). Scale bar: 50 μm.
(C) Percentage of cells with TDP-43^{mNLS}-Clover aggregates over time. Data points represent quantifications from 3 experiments. Mean ± SD. Dunnett's one-way ANOVA (ns, non-significant).
(D) Percentage of cells with compacted (orange), filamentous (green), or fragmented (gray) aggregates with time. *n* represents the total number of aggregates evaluated at each time point, from 3 experiments.
(E) Experimental outline of non-dividing TDP-43^{mNLS}-Clover cells exposed to 50 nM seeds over time. Doxycycline was removed after 2 days of culture to restrict TDP-43^{mNLS}-Clover expression in time (see F–I).
(F) Immunostaining of TDP-43^{mNLS}-Clover (green), phospho-TDP-43 (yellow), and DAPI (blue) at 2, 5, and 8 days post-seed exposure. Symbols indicate aggregate shapes (compacted, orange arrowhead; filamentous, green arrow; fragmented, white star). Scale bar: 50 μm.
(G) Percentage of cells with aggregates over time. Data points represent quantifications from 3 experiments. Mean ± SD. Dunnett's one-way ANOVA (*$p < 0.05$; ****$p < 0.0001$).
(H) Percentage of cells with compacted (orange), filamentous (green), or fragmented (gray) aggregates with time. *n* represents the total number of aggregates evaluated from 3 experiments.
(I) Time-lapse imaging of TDP-43^{mNLS}-Clover aggregates (green), followed over time from days 7 to 8 post-seed exposure. Scale bar: 20 μm.
See also Figures S7 and S8.

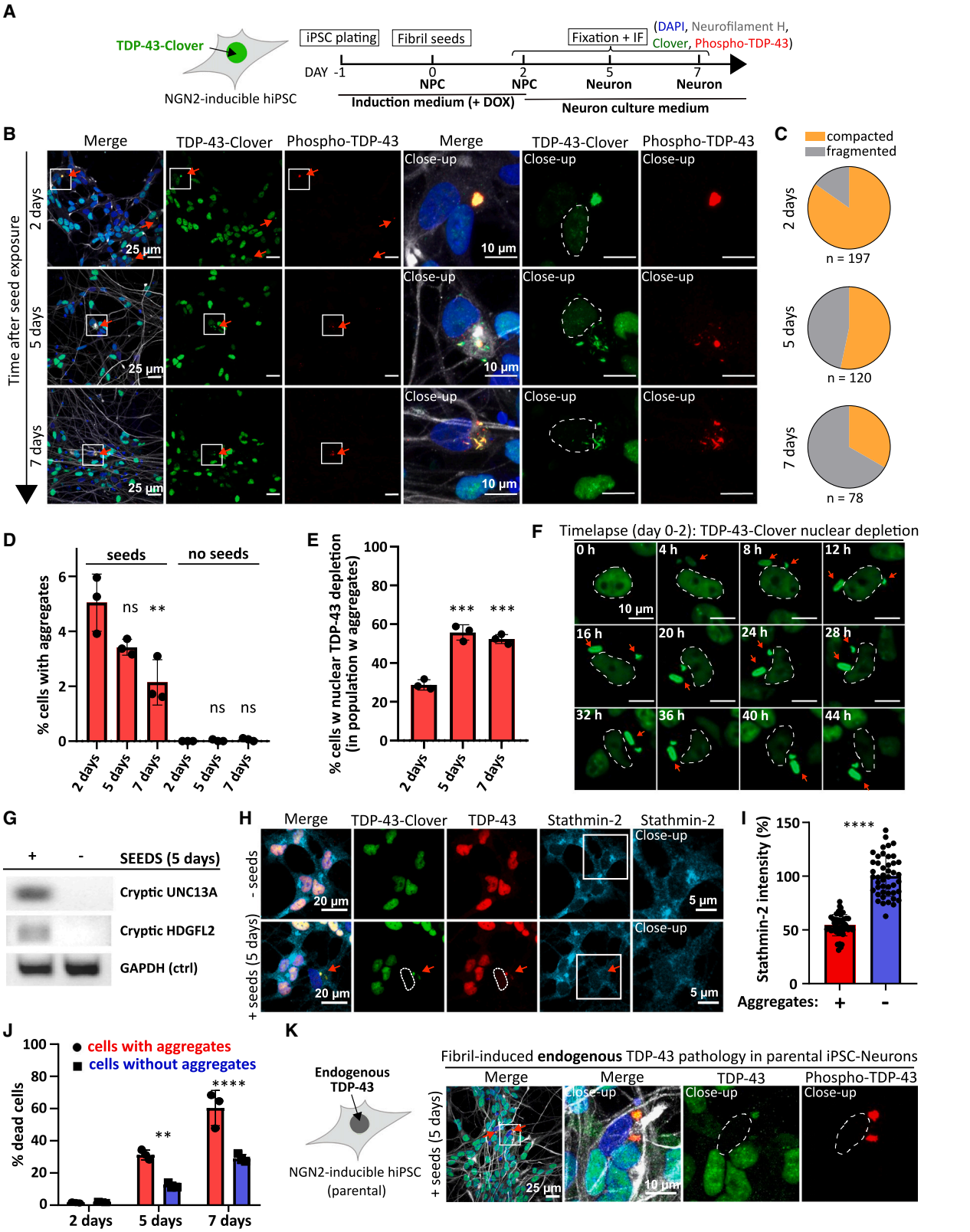

(legend on next page)

occurs in a templated fashion. Recent cryoelectron microscopy (cryo-EM) studies report that TDP-43 fibrils in patients with different disease subtypes have unique amyloid structures,[63–65] and recombinant fibrils composed of the TDP-43 LCD were previously reported to acquire yet a different amyloid fold.[23] Further work is needed to unravel the functional implications of these different amyloid structures.

TDP-43 nuclear depletion and loss of function in diseased cells contribute to pathogenesis.[66] We find that fibril seeds trigger endogenous TDP-43 to leave the nucleus and accumulate in cytoplasmic aggregates not only in human cells expressing fluorescently labeled TDP-43 but also in naive cells. The precise underlying mechanisms remain to be elucidated. TDP-43 might be "trapped" by aggregates as it shuttles to the cytoplasm[67,68] and consequently cannot return to the nucleus, causing gradual depletion of the nuclear TDP-43 pool. Likewise, the newly synthesized TDP-43 might be trapped by cytoplasmic aggregates immediately following translation, thus preventing its nuclear import. Alternatively, aggregates could trigger nuclear TDP-43 clearance indirectly by impairing importin β1-mediated nucleocytoplasmic transport.[69,70] Importantly, seeding ultimately caused TDP-43 nuclear loss of function including aberrant splicing—as revealed by cryptic exons in mRNA transcripts, such as the FTD-ALS gene *UNC13A*—hence recapitulating an essential disease feature.[47,48] Furthermore, the transcriptomic profile of cells with seeded TDP-43 pathology highlights widespread gene expression alterations, with upregulation of transcripts associated with neurodegenerative diseases and proteostasis and downregulation of known TDP-43 targets like *STMN2*. Hence, this dataset provides a valuable resource to further map the molecular underpinnings of TDP-43 proteinopathies.

Liquid TDP-43 condensates can be converted to a gel-like/aggregated state in response to stressors suggesting that TDP-43 droplets may act as reaction centers for the formation of pathological aggregates.[11,40,71] In contrast, fibril-induced aggregates of Clover-tagged TDP-43 displayed solid-like properties by FRAP, shortly after their formation (6 h post-exposure). Likewise, FLIM analysis demonstrated a fluorescence lifetime shift upon fibril treatment that is indicative of a transition toward a more condensed (aggregated) state. These data suggest that once a first amyloid aggregate (seed) is present in the cell, TDP-43 aggregation may propagate independently of liquid condensates. We previously demonstrated that recombinant aggregates of full-length TDP-43 or FUS induce liquid-like TDP-43 condensates as opposed to solid aggregates,[11] potentially because the amyloid core is buried within these full-length fibrils and not accessible to directly seed TDP-43 aggregation.[34] Hence, it would be valuable to compare fibrils produced from different TDP-43 variants/domains. Overall, we did not observe major differences in biophysical properties of cytoplasmic mutant and wild-type TDP-43 aggregates. However, TDP-43^{mNLS} aggregates grew larger with more striking morphologies, likely due to constant supply of cytoplasmic TDP-43.

Pathological heterogeneity is a key feature of ALS/FTD pathology.[29] Interestingly, aggregation of TDP-43-Clover induced by recombinant fibrils eventually also resulted in distinct aggregate morphologies. Our findings support that these various shapes are caused by progressive degradation of TDP-43 aggregates. First, seeded aggregation of TDP-43 resulted in upregulation and recruitment of protein degradation pathways, in line with efforts reporting activation of multiple proteostasis pathways in TDP-43 models and postmortem patient CNS.[53–57,72] Second, seed treatment combined with proteasome inhibitors in our cell model was sufficient to prevent time-dependent morphological changes in TDP-43-Clover aggregates. Finally, suppressing TDP-43-Clover expression promoted aggregate clearance that was associated with increased fragmentation. Hence, our findings suggest that different TDP-43 aggregate morphologies have a common origin and represent distinct stages in the

Figure 6. Fibrils induce cytoplasmic aggregation and nuclear loss of TDP-43 in differentiating iPSC neurons in a time-dependent manner

(A) Schematic outline of the seeding assay in iPSC-derived neurons expressing TDP-43^{WT}-Clover with sonicated recombinant TDP-43 LCD seeds (250 nM) directly added to the medium.

(B) Immunostaining of TDP-43^{WT}-Clover (green), phospho-TDP-43 (red), NF-H (gray), and DAPI (blue) at 2, 5, and 7 days post-seed treatment. Red arrows indicate TDP-43^{WT}-Clover aggregates. White dotted line outlines the nucleus. Scale bar overview: 25 μm; close up: 10 μm.

(C) Percentage of aggregates with compacted (orange) or fragmented (gray) morphology over time. *n* represents the total number of aggregates from 3 experiments.

(D) Percentage of cells with phosphorylated TDP-43^{WT}-Clover aggregates. Only living cells were considered for these quantifications. Data points represent different time exposures to the seeds from 3 experiments. Mean ± SD. One-way ANOVA followed by Sidak's test (ns, non-significant; $^{**}p < 0.01$).

(E) Percentage of cells with nuclear TDP-43 depletion relative to the total number of cells with aggregates. Data points represent different time exposures to the seeds from 3 experiments. Mean ± SD. Dunnett's one-way ANOVA ($^{***}p < 0.001$).

(F) 2-day time lapse of a human NPC following seed treatment. Red arrows point to TDP-43^{WT}-Clover aggregates. White dotted line outlines the nucleus. Scale bar: 10 μm.

(G) RT-PCR analysis of *de novo* cryptic RNA transcripts (*UNC13A* and *HDGFL2*) in TDP-43^{WT}-Clover iPSC neurons 5 days post-seed (or buffer control) treatment (250 nM). *GAPDH* transcript was used as PCR control.

(H) Immunostaining of TDP-43-Clover (green), TDP-43 (red), stathmin-2 (turquoise), and DAPI (blue) at 5 days post-seed treatment. Scale bar overview: 20 μm; close up: 5 μm.

(I) Quantification of stathmin-2 intensity in neurons with or without TDP-43 aggregates based on immunostaining in (H). Mean ± SD. Unpaired t test ($^{****}p < 0.0001$).

(J) Number of dead or dying neurons with (red) or without (blue) aggregates at 2, 5, or 7 days post-seed treatment (dead cells could be identified by their small and rounded/fragmented nucleus). Data points represent 3 experiments. Mean ± SD. Two-way ANOVA followed by Sidak's test ($^{**}p < 0.01$; $^{****}p < 0.0001$).

(K) Immunostaining of endogenous TDP-43 (green), phospho-TDP-43 (red), NF-H (gray), and DAPI (blue) at 5 days post-seed treatment (related to Figure S11). Red arrows indicate TDP-43 aggregates. White dotted line outlines the nucleus. Scale bar overview: 25 μm; close up: 10 μm.

See also Figures S9–S11.

degradation process. Cryo-EM to define the structure and mass spectrometry and investigate the protein composition of different aggregate types in our model will likely provide more insight. Brain extracts from ALS and different FTLD subtypes reportedly also induce distinct TDP-43 aggregate shapes in model systems, which have been linked to the presence of different proteopathic strains,[35,37,38] although these aggregates were not evaluated for extended periods in a time-dependent fashion. In light of our findings, it is plausible that TDP-43 strains from different disorders are differentially processed by the degradation machinery in different cell types, causing distinct presentations and progression rates of TDP-43 pathology. Additional work is thus needed to unravel the exact mechanisms underlying pathological heterogeneity in patients.

Recombinant TDP-43 LCD fibrils also induced TDP-43 pathology, including nuclear loss of function, in human iPSC-derived neurons. These features are typically not (fully) recapitulated in iPSC neurons with endogenous disease mutations, suggesting that additional "hits" may be required for the development of neuronal TDP-43 pathology.[73] In contrast with U2OS cells, fibrils in cultured neurons were spontaneously uptaken (no transfection) and induced cell death, potentially reflecting increased vulnerability to TDP-43 pathology as cells acquire a neuronal fate. Experiments aimed at uncovering aggregation-induced changes in the proteomic/transcriptomic landscape of neuronal versus non-neuronal cells will thus be highly valuable. It is also plausible that toxicity associated with TDP-43 pathology depends on the maturation/developmental stage of the neurons. Further assessment of such effects in older neuronal cultures will be of interest. While fibril seed uptake in differentiating TDP-43-Clover iPSC neurons was accompanied by substantial toxicity from day 7 post-seed treatment, yielding a relatively high baseline for cell death, this was reduced in non-engineered parental iPSC neurons. Regardless, toxicity was consistently more pronounced in neurons with aggregates, highlighting the detrimental consequences of TDP-43 mislocalization and aggregation on neuronal health.

The exact mechanisms that underlie mislocalization and aggregation of TDP-43, and ultimately its nuclear depletion, in neurodegenerative disorders remain poorly understood, partly due to a lack of physiological cellular models that reliably recapitulate TDP-43 pathology. We demonstrate that recombinant TDP-43 LCD fibrils trigger TDP-43 gain of toxicity and loss of function in cell lines and iPSC neurons in a reproducible fashion. This represents a valuable model of TDP-43 pathology—particularly in the context of sporadic disease—and a powerful tool to unravel disease mechanisms and screen potential drug candidates.

RESOURCE AVAILABILITY

Lead contact

Requests for further information, resources, and reagents should be directed to and will be fulfilled by the lead contact, Sandrine Da Cruz (sandrine.dacruz@kuleuven.be).

Materials availability

All unique/stable reagents generated in this study are available from the lead contact without restrictions.

Data and code availability

All data reported in this paper will be shared by the lead contact upon request. Any additional information required to reanalyze the data reported in this paper is available from the lead contact upon request. Raw gene expression data, including RNA and junction counts, are accessible via Gene Expression Omnibus (GEO) with the following accession number: GEO: GSE284828. For analysis of LAMP1-TDP-43 spatial distribution, the complete analysis pipeline and documentation are available at https://github.com/nicoperedo/LAMP1_distance_to_TDP43 (https://doi.org/10.5281/zenodo.14926087).

ACKNOWLEDGMENTS

We thank Axelle Kerstens from the Bio-Imaging Core (BIC) Leuven and the Advanced Optical Microscopy Centre Hasselt for imaging support. We acknowledge the VIB Nucleomics core for support with RNA-seq, the VIB Flow-Core Leuven for cell sorting, and the Biophysics Expertise Unit for fibril characterizations. We also thank Drs. Sonia Vazquez-Sanchez and Shan Lu for sharing the engineered TDP-43-Clover iPSC line, Dr. Hung Huy Nguyen for input on protein purifications, and Dr. Suresh Poovathingal for support in RNA-seq design. This work was supported by the KUL-STG grant, the FWO (Research Foundation-Flanders, G064721N), the Muscular Dystrophy Association (MDA, 962700), the Alzheimer Research Foundation (SAO) (grant SAO-FRA 20230035), and the Flanders Institute for Biotechnology (VIB) (grants to S.D.C.). Lifetime microscopy was made possible by FWO project grant G0H3716N. The Switch Laboratory was supported by an FWO project grant to F.R. (G0C3522N). J.R., B.K., and P.S. received an FWO PhD fellowship (1S15218N), an SAO-FRA pilot grant (20230042), and a scholarship from Hasselt University (BOF20OWB16), respectively. Graphical illustrations were generated with BioRender.com.

AUTHOR CONTRIBUTIONS

Conceptualization, J.R. and S.D.C.; methodology, J.R., G.Y., B.K., P.S., V.Z., N.P., M.R., and K.D.; investigation, J.R., B.K., P.S., G.Y., and V.Z.; formal analysis, J.R., B.K., G.Y., P.S., N.P., and K.D.; writing – original draft, J.R. and S.D.C.; writing – review & editing, J.R., B.K., J.S., F.R., V.Z., N.P., J.H., L.V.D.B., P.V.D., and S.D.C.; funding acquisition, J.H., J.S., F.R., and S.D.C.; supervision, F.R., J.S., J.H., and S.D.C.

DECLARATION OF INTERESTS

L.V.D.B. is head of the scientific advisory board of Augustine Therapeutics and is part of the investment advisory board of Droia Ventures (Meise, Belgium).

STAR★METHODS

Detailed methods are provided in the online version of this paper and include the following:

- KEY RESOURCES TABLE
- EXPERIMENTAL MODEL AND STUDY PARTICIPANT DETAILS
  - Cell culture
- METHOD DETAILS
  - Protein purification
  - Generation of recombinant TDP-43 LCD fibrils and seeds
  - Transmission electron microscopy (TEM) of recombinant fibrils
  - Congo red staining of recombinant fibrils
  - Fourier-transform infrared spectroscopy (FTIR)
  - Thioflavin-T (ThT) kinetic assays
  - Seeding assay in cultured cell lines
  - Seed transfection experiment with bortezomib/MG-132 treatment
  - Human iPSC culture, neuronal differentiation and seeding assay
  - Immunocytochemistry
  - Imaging and quantification of TDP-43 aggregation/mislocalization
  - Time-lapse fluorescence imaging
  - Fluorescence recovery after photobleaching (FRAP)
  - Fluorescence lifetime imaging microscopy (FLIM)

SUPPLEMENTAL INFORMATION

Supplemental information can be found online at https://doi.org/10.1016/j.neuron.2025.03.004.

Received: July 12, 2024
Revised: December 21, 2024
Accepted: March 3, 2025
Published: March 28, 2025

REFERENCES

1. Neumann, M., Sampathu, D.M., Kwong, L.K., Truax, A.C., Micsenyi, M.C., Chou, T.T., Bruce, J., Schuck, T., Grossman, M., Clark, C.M., et al. (2006). Ubiquitinated TDP-43 in frontotemporal lobar degeneration and amyotrophic lateral sclerosis. Science *314*, 130–133. https://doi.org/10.1126/science.1134108.
2. Taylor, J.P., Brown, R.H., and Cleveland, D.W. (2016). Decoding ALS: from genes to mechanism. Nature *539*, 197–206. https://doi.org/10.1038/nature20413.
3. Ling, S.-C., Polymenidou, M., and Cleveland, D.W. (2013). Converging mechanisms in ALS and FTD: disrupted RNA and protein homeostasis. Neuron *79*, 416–438. https://doi.org/10.1016/j.neuron.2013.07.033.
4. Nelson, P.T., Dickson, D.W., Trojanowski, J.Q., Jack, C.R., Boyle, P.A., Arfanakis, K., Rademakers, R., Alafuzoff, I., Attems, J., Brayne, C., et al. (2019). Limbic-predominant age-related TDP-43 encephalopathy (LATE): consensus working group report. Brain *142*, 1503–1527. https://doi.org/10.1093/brain/awz099.
5. Meneses, A., Koga, S., O'Leary, J., Dickson, D.W., Bu, G., and Zhao, N. (2021). TDP-43 Pathology in Alzheimer's Disease. Mol. Neurodegener. *16*, 84. https://doi.org/10.1186/s13024-021-00503-x.
6. Polymenidou, M., Lagier-Tourenne, C., Hutt, K.R., Huelga, S.C., Moran, J., Liang, T.Y., Ling, S.C., Sun, E., Wancewicz, E., Mazur, C., et al. (2011). Long pre-mRNA depletion and RNA missplicing contribute to neuronal vulnerability from loss of TDP-43. Nat. Neurosci. *14*, 459–468. https://doi.org/10.1038/nn.2779.
7. Tollervey, J.R., Curk, T., Rogelj, B., Briese, M., Cereda, M., Kayikci, M., König, J., Hortobágyi, T., Nishimura, A.L., Župunski, V., et al. (2011). Characterizing the RNA targets and position-dependent splicing regulation by TDP-43. Nat. Neurosci. *14*, 452–458. https://doi.org/10.1038/nn.2778.
8. Butti, Z., and Patten, S.A. (2018). RNA Dysregulation in Amyotrophic Lateral Sclerosis. Front. Genet. *9*, 712. https://doi.org/10.3389/fgene.2018.00712.
9. Piol, D., Robberechts, T., and Da Cruz, S. (2023). Lost in local translation: TDP-43 and FUS in axonal/neuromuscular junction maintenance and dysregulation in amyotrophic lateral sclerosis. Neuron *111*, 1355–1380. https://doi.org/10.1016/j.neuron.2023.02.028.
10. Lagier-Tourenne, C., Polymenidou, M., and Cleveland, D.W. (2010). TDP-43 and FUS/TLS: emerging roles in RNA processing and neurodegeneration. Hum. Mol. Genet. *19*, R46–R64. https://doi.org/10.1093/hmg/ddq137.
11. Gasset-Rosa, F., Lu, S., Yu, H., Chen, C., Melamed, Z., Guo, L., Shorter, J., Da Cruz, S., and Cleveland, D.W. (2019). Cytoplasmic TDP-43 De-mixing Independent of Stress Granules Drives Inhibition of Nuclear Import, Loss of Nuclear TDP-43, and Cell Death. Neuron *102*, 339–357.e7. https://doi.org/10.1016/j.neuron.2019.02.038.
12. Gopal, P.P., Nirschl, J.J., Klinman, E., and Holzbaur, E.L.F. (2017). Amyotrophic lateral sclerosis-linked mutations increase the viscosity of liquid-like TDP-43 RNP granules in neurons. Proc. Natl. Acad. Sci. USA *114*, E2466–E2475. https://doi.org/10.1073/pnas.1614462114.
13. Hallegger, M., Chakrabarti, A.M., Lee, F.C.Y., Lee, B.L., Amalietti, A.G., Odeh, H.M., Copley, K.E., Rubien, J.D., Portz, B., Kuret, K., et al. (2021). TDP-43 condensation properties specify its RNA-binding and regulatory repertoire. Cell *184*, 4680–4696.e22. https://doi.org/10.1016/j.cell.2021.07.018.
14. Maharana, S., Wang, J., Papadopoulos, D.K., Richter, D., Pozniakovsky, A., Poser, I., Bickle, M., Rizk, S., Guillén-Boixet, J., Franzmann, T.M., et al. (2018). RNA buffers the phase separation behavior of prion-like RNA binding proteins. Science *360*, 918–921. https://doi.org/10.1126/science.aar7366.
15. Conicella, A.E., Zerze, G.H., Mittal, J., and Fawzi, N.L. (2016). ALS Mutations Disrupt Phase Separation Mediated by α-Helical Structure in the TDP-43 Low-Complexity C-Terminal Domain. Structure *24*, 1537–1549. https://doi.org/10.1016/j.str.2016.07.007.
16. McGurk, L., Gomes, E., Guo, L., Mojsilovic-Petrovic, J., Tran, V., Kalb, R.G., Shorter, J., and Bonini, N.M. (2018). Poly(ADP-Ribose) Prevents Pathological Phase Separation of TDP-43 by Promoting Liquid Demixing and Stress Granule Localization. Mol. Cell *71*, 703–717.e9. https://doi.org/10.1016/j.molcel.2018.07.002.
17. Pakravan, D., Michiels, E., Bratek-Skicki, A., De Decker, M., Van Lindt, J., Alsteens, D., Derclaye, S., Van Damme, P., Schymkowitz, J., Rousseau, F., et al. (2021). Liquid-Liquid Phase Separation Enhances TDP-43 LCD Aggregation but Delays Seeded Aggregation. Biomolecules *11*, 548. https://doi.org/10.3390/biom11040548.
18. Gruijs da Silva, L.A., Simonetti, F., Hutten, S., Riemenschneider, H., Sternburg, E.L., Pietrek, L.M., Gebel, J., Dötsch, V., Edbauer, D., Hummer, G., et al. (2022). Disease-linked TDP-43 hyperphosphorylation suppresses TDP-43 condensation and aggregation. EMBO J. *41*, e108443. https://doi.org/10.15252/embj.2021108443.
19. Keating, S.S., Bademosi, A.T., San Gil, R., and Walker, A.K. (2023). Aggregation-prone TDP-43 sequesters and drives pathological transitions of free nuclear TDP-43. Cell. Mol. Life Sci. *80*, 95. https://doi.org/10.1007/s00018-023-04739-2.
20. Boeynaems, S., Alberti, S., Fawzi, N.L., Mittag, T., Polymenidou, M., Rousseau, F., Schymkowitz, J., Shorter, J., Wolozin, B., Van Den Bosch, L., et al. (2018). Protein Phase Separation: A New Phase in Cell Biology. Trends Cell Biol. *28*, 420–435. https://doi.org/10.1016/j.tcb.2018.02.004.
21. Koehler, L.C., Grese, Z.R., Bastos, A.C.S., Mamede, L.D., Heyduk, T., and Ayala, Y.M. (2022). TDP-43 Oligomerization and Phase Separation Properties Are Necessary for Autoregulation. Front. Neurosci. *16*, 818655. https://doi.org/10.3389/fnins.2022.818655.
22. Guenther, E.L., Cao, Q., Trinh, H., Lu, J., Sawaya, M.R., Cascio, D., Boyer, D.R., Rodriguez, J.A., Hughes, M.P., and Eisenberg, D.S. (2018). Atomic structures of TDP-43 LCD segments and insights into reversible or pathogenic aggregation. Nat. Struct. Mol. Biol. *25*, 463–471. https://doi.org/10.1038/s41594-018-0064-2.
23. Li, Q., Babinchak, W.M., and Surewicz, W.K. (2021). Cryo-EM structure of amyloid fibrils formed by the entire low complexity domain of TDP-43. Nat. Commun. *12*, 1620. https://doi.org/10.1038/s41467-021-21912-y.
24. Johnson, B.S., Snead, D., Lee, J.J., McCaffery, J.M., Shorter, J., and Gitler, A.D. (2009). TDP-43 is intrinsically aggregation-prone, and amyotrophic lateral sclerosis-linked mutations accelerate aggregation and increase toxicity. J. Biol. Chem. *284*, 20329–20339. https://doi.org/10.1074/jbc.M109.010264.

25. Mann, J.R., Gleixner, A.M., Mauna, J.C., Gomes, E., DeChellis-Marks, M.R., Needham, P.G., Copley, K.E., Hurtle, B., Portz, B., Pyles, N.J., et al. (2019). RNA Binding Antagonizes Neurotoxic Phase Transitions of TDP-43. Neuron *102*, 321–338.e8. https://doi.org/10.1016/j.neuron.2019.01.048.

26. Alberti, S., and Hyman, A.A. (2021). Biomolecular condensates at the nexus of cellular stress, protein aggregation disease and ageing. Nat. Rev. Mol. Cell Biol. *22*, 196–213. https://doi.org/10.1038/s41580-020-00326-6.

27. Babinchak, W.M., Haider, R., Dumm, B.K., Sarkar, P., Surewicz, K., Choi, J.K., and Surewicz, W.K. (2019). The role of liquid-liquid phase separation in aggregation of the TDP-43 low-complexity domain. J. Biol. Chem. *294*, 6306–6317. https://doi.org/10.1074/jbc.RA118.007222.

28. Arai, T., Hasegawa, M., Akiyama, H., Ikeda, K., Nonaka, T., Mori, H., Mann, D., Tsuchiya, K., Yoshida, M., Hashizume, Y., et al. (2006). TDP-43 is a component of ubiquitin-positive tau-negative inclusions in frontotemporal lobar degeneration and amyotrophic lateral sclerosis. Biochem. Biophys. Res. Commun. *351*, 602–611. https://doi.org/10.1016/j.bbrc.2006.10.093.

29. Kawakami, I., Arai, T., and Hasegawa, M. (2019). The basis of clinicopathological heterogeneity in TDP-43 proteinopathy. Acta Neuropathol. *138*, 751–770. https://doi.org/10.1007/s00401-019-02077-x.

30. Laferrière, F., Maniecka, Z., Pérez-Berlanga, M., Hruska-Plochan, M., Gilhespy, L., Hock, E.M., Wagner, U., Afroz, T., Boersema, P.J., Barmettler, G., et al. (2019). TDP-43 extracted from frontotemporal lobar degeneration subject brains displays distinct aggregate assemblies and neurotoxic effects reflecting disease progression rates. Nat. Neurosci. *22*, 65–77. https://doi.org/10.1038/s41593-018-0294-y.

31. Masters, C.L., Kril, J.J., Halliday, G.M., Pamphlett, R., Collins, S., Hill, A.F., and McLean, C. (2011). Overview and recent advances in neuropathology. Part 2: Neurodegeneration. Pathology *43*, 93–102. https://doi.org/10.1097/PAT.0b013e3283426eee.

32. Brettschneider, J., Del Tredici, K., Toledo, J.B., Robinson, J.L., Irwin, D.J., Grossman, M., Suh, E., Van Deerlin, V.M., Wood, E.M., Baek, Y., et al. (2013). Stages of pTDP-43 pathology in amyotrophic lateral sclerosis. Ann. Neurol. *74*, 20–38. https://doi.org/10.1002/ana.23937.

33. Brettschneider, J., Del Tredici, K., Irwin, D.J., Grossman, M., Robinson, J.L., Toledo, J.B., Fang, L., Van Deerlin, V.M., Ludolph, A.C., Lee, V.M.Y., et al. (2014). Sequential distribution of pTDP-43 pathology in behavioral variant frontotemporal dementia (bvFTD). Acta Neuropathol. *127*, 423–439. https://doi.org/10.1007/s00401-013-1238-y.

34. Kumar, S.T., Nazarov, S., Porta, S., Maharjan, N., Cendrowska, U., Kabani, M., Finamore, F., Xu, Y., Lee, V.M.Y., and Lashuel, H.A. (2023). Seeding the aggregation of TDP-43 requires post-fibrillization proteolytic cleavage. Nat. Neurosci. *26*, 983–996. https://doi.org/10.1038/s41593-023-01341-4.

35. De Rossi, P., Lewis, A.J., Furrer, J., De Vos, L., Demeter, T., Zbinden, A., Zhong, W., Wiersma, V.I., Scialo, C., Weber, J., et al. (2021). FTLD-TDP assemblies seed neoaggregates with subtype-specific features via a prion-like cascade. EMBO Rep. *22*, e53877. https://doi.org/10.15252/embr.202153877.

36. Nonaka, T., Masuda-Suzukake, M., Arai, T., Hasegawa, Y., Akatsu, H., Obi, T., Yoshida, M., Murayama, S., Mann, D.M.A., Akiyama, H., et al. (2013). Prion-like properties of pathological TDP-43 aggregates from diseased brains. Cell Rep. *4*, 124–134. https://doi.org/10.1016/j.celrep.2013.06.007.

37. Smethurst, P., Newcombe, J., Troakes, C., Simone, R., Chen, Y.R., Patani, R., and Sidle, K. (2016). In vitro prion-like behaviour of TDP-43 in ALS. Neurobiol. Dis. *96*, 236–247. https://doi.org/10.1016/j.nbd.2016.08.007.

38. Porta, S., Xu, Y., Lehr, T., Zhang, B., Meymand, E., Olufemi, M., Stieber, A., Lee, E.B., Trojanowski, J.Q., and Lee, V.M.Y. (2021). Distinct brain-derived TDP-43 strains from FTLD-TDP subtypes induce diverse morphological TDP-43 aggregates and spreading patterns in vitro and in vivo. Neuropathol. Appl. Neurobiol. *47*, 1033–1049. https://doi.org/10.1111/nan.12732.

39. Porta, S., Xu, Y., Restrepo, C.R., Kwong, L.K., Zhang, B., Brown, H.J., Lee, E.B., Trojanowski, J.Q., and Lee, V.M.Y. (2018). Patient-derived frontotemporal lobar degeneration brain extracts induce formation and spreading of TDP-43 pathology in vivo. Nat. Commun. *9*, 4220. https://doi.org/10.1038/s41467-018-06548-9.

40. Lu, S., Hu, J., Arogundade, O.A., Goginashvili, A., Vazquez-Sanchez, S., Diedrich, J.K., Gu, J., Blum, J., Oung, S., Ye, Q., et al. (2022). Heat-shock chaperone HSPB1 regulates cytoplasmic TDP-43 phase separation and liquid-to-gel transition. Nat. Cell Biol. *24*, 1378–1393. https://doi.org/10.1038/s41556-022-00988-8.

41. Chilumuri, A., Markiv, A., and Milton, N.G.N. (2014). Immunocytochemical staining of endogenous nuclear proteins with the HIS-1 anti-poly-histidine monoclonal antibody: a potential source of error in His-tagged protein detection. Acta Histochem. *116*, 1022–1028. https://doi.org/10.1016/j.acthis.2014.04.006.

42. Joron, K., Viegas, J.O., Haas-Neill, L., Bier, S., Drori, P., Dvir, S., Lim, P.S.L., Rauscher, S., Meshorer, E., and Lerner, E. (2023). Fluorescent protein lifetimes report densities and phases of nuclear condensates during embryonic stem-cell differentiation. Nat. Commun. *14*, 4885. https://doi.org/10.1038/s41467-023-40647-6.

43. Coucke, Q., Parveen, N., Fernández, G.S., Qian, C., Hofkens, J., Debyser, Z., and Hendrix, J. (2023). Particle-based phasor-FLIM-FRET resolves protein-protein interactions inside single viral particles. Biophys. Rep. (N Y) *3*, 100122. https://doi.org/10.1016/j.bpr.2023.100122.

44. Digman, M.A., Caiolfa, V.R., Zamai, M., and Gratton, E. (2008). The phasor approach to fluorescence lifetime imaging analysis. Biophys. J. *94*, L14–L16. https://doi.org/10.1529/biophysj.107.120154.

45. Ling, J.P., Pletnikova, O., Troncoso, J.C., and Wong, P.C. (2015). TDP-43 repression of nonconserved cryptic exons is compromised in ALS-FTD. Science *349*, 650–655. https://doi.org/10.1126/science.aab0983.

46. Melamed, Z., López-Erauskin, J., Baughn, M.W., Zhang, O., Drenner, K., Sun, Y., Freyermuth, F., McMahon, M.A., Beccari, M.S., Artates, J.W., et al. (2019). Premature polyadenylation-mediated loss of stathmin-2 is a hallmark of TDP-43-dependent neurodegeneration. Nat. Neurosci. *22*, 180–190. https://doi.org/10.1038/s41593-018-0293-z.

47. Ma, X.R., Prudencio, M., Koike, Y., Vatsavayai, S.C., Kim, G., Harbinski, F., Briner, A., Rodriguez, C.M., Guo, C., Akiyama, T., et al. (2022). TDP-43 represses cryptic exon inclusion in the FTD–ALS gene UNC13A. Nature *603*, 124–130. https://doi.org/10.1038/s41586-022-04424-7.

48. Brown, A.L., Wilkins, O.G., Keuss, M.J., Hill, S.E., Zanovello, M., Lee, W.C., Bampton, A., Lee, F.C.Y., Masino, L., Qi, Y.A., et al. (2022). TDP-43 loss and ALS-risk SNPs drive mis-splicing and depletion of UNC13A. Nature *603*, 131–137. https://doi.org/10.1038/s41586-022-04436-3.

49. Humphrey, J., Venkatesh, S., Hasan, R., Herb, J.T., de Paiva Lopes, K., Küçükali, F., Byrska-Bishop, M., Evani, U.S., Narzisi, G., Fagegaltier, D., et al. (2023). Integrative transcriptomic analysis of the amyotrophic lateral sclerosis spinal cord implicates glial activation and suggests new risk genes. Nat. Neurosci. *26*, 150–162. https://doi.org/10.1038/s41593-022-01205-3.

50. Tanaka, H., Shimazawa, M., Kimura, M., Takata, M., Tsuruma, K., Yamada, M., Takahashi, H., Hozumi, I., Niwa, J., Iguchi, Y., et al. (2012). The potential of GPNMB as novel neuroprotective factor in amyotrophic lateral sclerosis. Sci. Rep. *2*, 573. https://doi.org/10.1038/srep00573.

51. Oeckl, P., Weydt, P., Thal, D.R., Weishaupt, J.H., Ludolph, A.C., and Otto, M. (2020). Proteomics in cerebrospinal fluid and spinal cord suggests UCHL1, MAP2 and GPNMB as biomarkers and underpins importance of transcriptional pathways in amyotrophic lateral sclerosis. Acta Neuropathol. *139*, 119–134. https://doi.org/10.1007/s00401-019-02093-x.

52. Bordi, M., De Cegli, R., Testa, B., Nixon, R.A., Ballabio, A., and Cecconi, F. (2021). A gene toolbox for monitoring autophagy transcription. Cell Death Dis. *12*, 1044. https://doi.org/10.1038/s41419-021-04121-9.

53. Nakano, T., Nakaso, K., Nakashima, K., and Ohama, E. (2004). Expression of ubiquitin-binding protein p62 in ubiquitin-immunoreactive intraneuronal inclusions in amyotrophic lateral sclerosis with dementia: Analysis of five autopsy cases with broad clinicopathological spectrum. Acta Neuropathol. *107*, 359–364. https://doi.org/10.1007/s00401-004-0821-7.

54. Scotter, E.L., Vance, C., Nishimura, A.L., Lee, Y.B., Chen, H.J., Urwin, H., Sardone, V., Mitchell, J.C., Rogelj, B., Rubinsztein, D.C., et al. (2014). Differential roles of the ubiquitin proteasome system and autophagy in the clearance of soluble and aggregated TDP-43 species. J. Cell Sci. *127*, 1263–1278. https://doi.org/10.1242/jcs.140087.

55. Cicardi, M.E., Cristofani, R., Rusmini, P., Meroni, M., Ferrari, V., Vezzoli, G., Tedesco, B., Piccolella, M., Messi, E., Galbiati, M., et al. (2018). Tdp-25 Routing to Autophagy and Proteasome Ameliorates its Aggregation in Amyotrophic Lateral Sclerosis Target Cells. Sci. Rep. *8*, 12390. https://doi.org/10.1038/s41598-018-29658-2.

56. Barmada, S.J., Serio, A., Arjun, A., Bilican, B., Daub, A., Ando, D.M., Tsvetkov, A., Pleiss, M., Li, X., Peisach, D., et al. (2014). Autophagy induction enhances TDP43 turnover and survival in neuronal ALS models. Nat. Chem. Biol. *10*, 677–685. https://doi.org/10.1038/nchembio.1563.

57. Riemenschneider, H., Guo, Q., Bader, J., Frottin, F., Farny, D., Kleinberger, G., Haass, C., Mann, M., Hartl, F.U., Baumeister, W., et al. (2022). Gel-like inclusions of C-terminal fragments of TDP-43 sequester stalled proteasomes in neurons. EMBO Rep. *23*, e53890. https://doi.org/10.15252/embr.202153890.

58. Fernandopulle, M.S., Prestil, R., Grunseich, C., Wang, C., Gan, L., and Ward, M.E. (2018). Transcription Factor–Mediated Differentiation of Human iPSCs into Neurons. Curr. Protoc. Cell Biol. *79*, e51. https://doi.org/10.1002/cpcb.51.

59. De Boer, E.M.J., Orie, V.K., Williams, T., Baker, M.R., De Oliveira, H.M., Polvikoski, T., Silsby, M., Menon, P., Van Den Bos, M., Halliday, G.M., et al. (2020). TDP-43 proteinopathies: A new wave of neurodegenerative diseases. J. Neurol. Neurosurg. Psychiatry *92*, 86–95. https://doi.org/10.1136/jnnp-2020-322983.

60. Lynch, E.M., Pittman, S., Daw, J., Ikenaga, C., Chen, S., Dhavale, D.D., Jackrel, M.E., Ayala, Y.M., Kotzbauer, P., Ly, C.V., et al. (2024). Seeding-competent TDP-43 persists in human patient and mouse muscle. Sci. Transl. Med. *16*, eadp5730. https://doi.org/10.1126/scitranslmed.adp5730.

61. Smethurst, P., Risse, E., Tyzack, G.E., Mitchell, J.S., Taha, D.M., Chen, Y.-R., Newcombe, J., Collinge, J., Sidle, K., and Patani, R. (2020). Distinct responses of neurons and astrocytes to TDP-43 proteinopathy in amyotrophic lateral sclerosis. Brain *143*, 430–440. https://doi.org/10.1093/brain/awz419.

62. Tamaki, Y., Ross, J.P., Alipour, P., Castonguay, C.-É., Li, B., Catoire, H., Rochefort, D., Urushitani, M., Takahashi, R., Sonnen, J.A., et al. (2023). Spinal cord extracts of amyotrophic lateral sclerosis spread TDP-43 pathology in cerebral organoids. PLoS Genet. *19*, e1010606. https://doi.org/10.1371/journal.pgen.1010606.

63. Arseni, D., Hasegawa, M., Murzin, A.G., Kametani, F., Arai, M., Yoshida, M., and Ryskeldi-Falcon, B. (2022). Structure of pathological TDP-43 filaments from ALS with FTLD. Nature *601*, 139–143. https://doi.org/10.1038/s41586-021-04199-3.

64. Arseni, D., Chen, R., Murzin, A.G., Peak-Chew, S.Y., Garringer, H.J., Newell, K.L., Kametani, F., Robinson, A.C., Vidal, R., Ghetti, B., et al. (2023). TDP-43 forms amyloid filaments with a distinct fold in type A FTLD-TDP. Nature *620*, 898–903. https://doi.org/10.1038/s41586-023-06405-w.

65. Arseni, D., Nonaka, T., Jacobsen, M.H., Murzin, A.G., Cracco, L., Peak-Chew, S.Y., Garringer, H.J., Kawakami, I., Suzuki, H., Onaya, M., et al. (2024). Heteromeric amyloid filaments of ANXA11 and TDP-43 in FTLD-TDP type C. Nature *634*, 662–668. https://doi.org/10.1038/s41586-024-08024-5.

66. Vanden Broeck, L., Callaerts, P., and Dermaut, B. (2014). TDP-43-mediated neurodegeneration: Towards a loss-of-function hypothesis? Trends Mol. Med. *20*, 66–71. https://doi.org/10.1016/j.molmed.2013.11.003.

67. Ayala, Y.M., Zago, P., D'Ambrogio, A., Xu, Y.F., Petrucelli, L., Buratti, E., and Baralle, F.E. (2008). Structural determinants of the cellular localization and shuttling of TDP-43. J. Cell Sci. *121*, 3778–3785. https://doi.org/10.1242/jcs.038950.

68. Duan, L., Zaepfel, B.L., Aksenova, V., Dasso, M., Rothstein, J.D., Kalab, P., and Hayes, L.R. (2022). Nuclear RNA binding regulates TDP-43 nuclear localization and passive nuclear export. Cell Rep. *40*, 111106. https://doi.org/10.1016/j.celrep.2022.111106.

69. Chou, C.C., Zhang, Y., Umoh, M.E., Vaughan, S.W., Lorenzini, I., Liu, F., Sayegh, M., Donlin-Asp, P.G., Chen, Y.H., Duong, D.M., et al. (2018). TDP-43 pathology disrupts nuclear pore complexes and nucleocytoplasmic transport in ALS/FTD. Nat. Neurosci. *21*, 228–239. https://doi.org/10.1038/s41593-017-0047-3.

70. Khalil, B., Linsenmeier, M., Smith, C.L., Shorter, J., and Rossoll, W. (2024). Nuclear-import receptors as gatekeepers of pathological phase transitions in ALS/FTD. Mol. Neurodegener. *19*, 8. https://doi.org/10.1186/s13024-023-00698-1.

71. Carey, J.L., and Guo, L. (2022). Liquid-Liquid Phase Separation of TDP-43 and FUS in Physiology and Pathology of Neurodegenerative Diseases. Front. Mol. Biosci. *9*, 826719. https://doi.org/10.3389/fmolb.2022.826719.

72. Pozzi, S., Codron, P., Soucy, G., Renaud, L., Cordeau, P.J., Dutta, K., Bareil, C., and Julien, J.P. (2020). Monoclonal full-length antibody against TAR DNA binding protein 43 reduces related proteinopathy in neurons. JCI Insight *5*, e140420. https://doi.org/10.1172/jci.insight.140420.

73. Fazal, R., Boeynaems, S., Swijsen, A., De Decker, M., Fumagalli, L., Moisse, M., Vanneste, J., Guo, W., Boon, R., Vercruysse, T., et al. (2021). HDAC6 inhibition restores TDP-43 pathology and axonal transport defects in human motor neurons with TARDBP mutations. EMBO J. *40*, e106177. https://doi.org/10.15252/embj.2020106177.

74. Wang, C., Ward, M.E., Chen, R., Liu, K., Tracy, T.E., Chen, X., Xie, M., Sohn, P.D., Ludwig, C., Meyer-Franke, A., et al. (2017). Scalable Production of iPSC-Derived Human Neurons to Identify Tau-Lowering Compounds by High-Content Screening. Stem Cell Rep. *9*, 1221–1233. https://doi.org/10.1016/j.stemcr.2017.08.019.

75. Lam, A.J., St-Pierre, F., Gong, Y., Marshall, J.D., Cranfill, P.J., Baird, M.A., McKeown, M.R., Wiedenmann, J., Davidson, M.W., Schnitzer, M.J., et al. (2012). Improving FRET dynamic range with bright green and red fluorescent proteins. Nat. Methods *9*, 1005–1012. https://doi.org/10.1038/nmeth.2171.

76. Boeynaems, S., De Decker, M., Tompa, P., and Van Den Bosch, L. (2017). Arginine-rich Peptides Can Actively Mediate Liquid-liquid Phase Separation. Bio Protoc. *7*, e2525. https://doi.org/10.21769/BioProtoc.2525.

77. Schrimpf, W., Barth, A., Hendrix, J., and Lamb, D.C. (2018). PAM: A Framework for Integrated Analysis of Imaging, Single-Molecule, and Ensemble Fluorescence Data. Biophys. J. *114*, 1518–1528. https://doi.org/10.1016/j.bpj.2018.02.035.

STAR★METHODS

KEY RESOURCES TABLE

REAGENT or RESOURCE	SOURCE	IDENTIFIER
Antibodies		
TDP-43 antibody	Proteintech	10782-2-AP; RRID: AB_615042
Phospho-TDP-43 antibody	BioLegend	829901; RRID: AB_2564934
FUS antibody	Bethyl Laboratories	A300-302A; RRID: AB_309445
hnRNPA2/B1 antibody	Santa Cruz	sc-374053
Polyhistidine antibody	Sigma Aldrich	H1029; RRID: AB_260015
Ubiquitin antibody	Santa Cruz	sc-8017; RRID: AB_2762364
p62 antibody	Progen	GP62-C; RRID: AB_2687531
PSMA1 antibody	Invitrogen	PA1-963; RRID: AB_2171381
PSMC4 antibody	Arigo Biolaboratories	ARG43994050
LAMP1 antibody	DSHB	H4A3
EEA1 antibody	Sigma Aldrich	E4156; RRID: AB_609870
Neurofilament H antibody	Merck	AB5539; RRID: AB_11212161
Stathmin-2 antibody	Proteintech	#67204-1-Ig; RRID: AB_2882497
Tau antibody	Invitrogen	#MN1000; RRID: AB_2314654
NeuN antibody	Genetex	#GTX133127
MAP2 antibody	Novus Bio	#NB300-213; RRID: AB_2138178
Vinculin antibody	Sigma	#V9131; RRID: AB_477629
Alexa Fluor® 488 AffiniPure Donkey Anti-Rabbit IgG (H+L)	Jackson ImmunoResearch	711-545-152; RRID: AB_2313584
Alexa Fluor® 647 AffiniPure Donkey Anti-Rabbit IgG (H+L)	Jackson ImmunoResearch	711-605-152; RRID: AB_2492288
Cy3-AffiniPure Donkey Anti-Rabbit IgG (H+L)	Jackson ImmunoResearch	711-165-152; RRID: AB_2307443
Alexa Fluor 647-AffiniPure Donkey Anti-Guinea Pig IgG (H+L)	Jackson ImmunoResearch	706-605-148; RRID: AB_2340476
Cy™3 AffiniPure Donkey Anti-Rat IgG (H+L)	Jackson ImmunoResearch	712-165-153; RRID: AB_2340667
Alexa Fluor® 647 AffiniPure Donkey Anti-Mouse IgG (H+L)	Jackson ImmunoResearch	715-605-151; RRID: AB_2340863
AffiniPure Donkey Anti-Chicken IgY (IgG) (H+L), 0.5mg, Cy3	Jackson ImmunoResearch	703-165-155; RRID: AB_2340363
Goat anti-Rat IgG (H+L) Cross-Adsorbed Secondary Antibody, Alexa Fluor™ 647	ThermoFisher	A-21247; RRID: AB_141778
Bacterial and virus strains		
Escherichia coli BL21 STAR (DE3) cells	ThermoFisher	C601003
Chemicals, peptides, and recombinant proteins		
DMEM	Gibco	21969035
Fetal bovine serum	Gibco	A5256701
Matrigel	VWR	734-1440
Essential 8 medium	Thermofisher	A2858501
PLO	Sigma	P4638
DMEM/F12	Gibco	11330032
N2 supplement	Gibco	17502048
Non-essential amino acids	Gibco	11140050
L-glutamine	Gibco	25030081
Y-27632 dihydrochloride ROCK inhibitor	Selleck Chemicals	S1049
Doxycycline	Sigma Aldrich	D9891
Neurobasal	Gibco	21103049
B-27 supplement serum free	Gibco	17504044
Neurotrophin-3 (NT-3)	ThermoFisher	PHC7036

(*Continued on next page*)

Continued

REAGENT or RESOURCE	SOURCE	IDENTIFIER
Mouse laminin	Gibco	23017015
BDNF	PeproTech	450-02
Isopropyl-β-D-1-thiogalactopyranoside (IPTG)	Merck	137064
EDTA-free protease inhibitor cocktail	Roche	4693132001
Imidazole	Millipore	104716
Coomassie Instant Blue	Abcam	ab119211
LB broth (Lennox)	Sigma	L3022
Tris base	ThermoFisher	10103203
Sodium Chloride	Sigma	S7653
DTT	ThermoFisher	R0861
Urea	Sigma	U5378
MES	Merck	M3671
Thioflavin T (ThT)	Merck	T3516
Lipofectamine-3000	Invitrogen	L3000001
Palbociclib	ApexBio	PD0332991
Bortezomib	Sigma Aldrich	5.04314
MG-132	Sigma Aldrich	474790
DAPI	Merck	N/A
CellTracker Deep Red dye	Invitrogen	C34565
Cell Tracking Red dye	Abcam	ab269446
FluoroBrite DMEM	A1896701	Gibco
Neurobasal without phenol red	Gibco	12348017
TRIzol reagent	Invitrogen	15596026
DNAse	Invitrogen	18068015
Critical commercial assays		
High-capacity reverse transcription kit	Applied Biosystems	4368814
Q5 High-Fidelity DNA polymerase kit	NEB	M0491
innuPREP RNA mini kit 2.0	Innuscreen GmbH	845-KS-2040010
Experimental models: Cell lines		
i3N iPSCs	Fernandopulle et al.[58]	N/A
Human TDP-43mNLS-Clover inducible U2OS	Gasset-Rosa et al.[11]	N/A
Human U2OS	ATCC	Cat# HTB-96
Oligonucleotides		
UNC13A Cryptic Forward: TGGATGGAGAGATGGAACCT	IDT	N/A
UNC13A Cryptic Reverse: GGGCTGTCTCATCGTAGTAAAC	IDT	N/A
HDGFL2 Cryptic Forward: AAGACGCCTGCGCTAAAGAT	IDT	N/A
HDGFL2 Cryptic Reverse: GCTTCCCTCCCTTCTGATGC	IDT	N/A
GPSM2 Cryptic Forward: AGTGGACATGTGGTGGTAAGAA	IDT	N/A
GPSM2 Cryptic Reverse: GCTTCAAAGAATGACACGCCA	IDT	N/A
ATG4B Cryptic Forward: TGTGTCTGGATGTGAGCGTG	IDT	N/A
ATG4B Cryptic Reverse: TCTAGGGACAGGTTCAGGACG	IDT	N/A
EPB41L4A Cryptic Forward: CAGTGTTGACGGGACAGG	IDT	N/A
EPB41L4A Cryptic Reverse: TGACATCGAGTCACCTTAC	IDT	N/A
PFKP Cryptic Forward: CTGAGCTCCGACACATCAGAAG	IDT	N/A
PFKP Cryptic Reverse: TCCTCCAGCAGCCCACTC	IDT	N/A
AGRN Cryptic Forward: CAGAGCTGCGTGTCCGTGATC	IDT	N/A
AGRN Cryptic Reverse: GGCTGCGGTGATATTGTCCTG	IDT	N/A
GAPDH Forward: GAAGGTGAAGGTCGGAGTC	IDT	N/A

(*Continued on next page*)

Continued		
REAGENT or RESOURCE	SOURCE	IDENTIFIER
GAPDH Reverse: GAAGATGGTGATGGGATTTC	IDT	N/A
Recombinant DNA		
pJ411_His-TDP43_LCD	Addgene	98669
pLenti_CMV_TDP-43^{WT}-Clover	This paper	N/A
Software and algorithms		
FIJI (ImageJ)	NIH	https://imagej.net/software/fiji/downloads
GraphPad prism	GraphPad	https://www.graphpad.com/scientific-software/prism/
Harmony High-content imaging and analysis software	PerkinElmer	N/A
NIS Elements Advanced Research software	Nikon	https://www.microscope.healthcare.nikon.com/products/software/nis-elements/nis-elements-advanced-research
MATLAB	MathWorks	https://nl.mathworks.com/products/matlab.html
Zen Black 2.3 SP1	ZEISS	https://www.micro-shop.zeiss.com/en/us/softwarefinder/software-categories/zen-black/zen-black-system/
Symphotime software	PicoQuant	https://www.picoquant.com/products/category/software
SnapGene	Snapgene	https://www.snapgene.com/
BioRender	BioRender	https://biorender.com/
Inkscape	Inkscape	https://inkscape.org/
Other		
96-well imaging plate (PhenoPlate)	PerkinElmer	6055802
Glass-bottom 8-well chamber slides	Ibidi	80827
HisTrap HP column	Cytiva	17524801
Superdex-200 16-600 size-exclusion column	Cytiva	28989335
Äkta Pure protein purification system	Cytiva	N/A
TEM copper grid	Ted Pella Inc.	01753-F
Microplate Shaker/Incubator PV-PVC	Provocell™	N/A
Branson 450 Digital Sonifier – Probe sonicator	Branson	N/A
Bioruptor pico	Diagenode	N/A
JEM 1400 elecron microscope	JEOL	N/A
FluoStar Omega plate reader	BMG Labtech	N/A
Operetta CLS microscope	PerkinElmer	N/A
Nikon A1R Eclipse TiE confocal microscope	Nikon	N/A
Zeiss LSM 880 confocal microscope	Zeiss	N/A

EXPERIMENTAL MODEL AND STUDY PARTICIPANT DETAILS

Cell culture

Genetically engineered inducible TDP-43^{mNLS}-Clover U2OS cells were previously published.[11] U2OS cells were cultured in DMEM (Gibco, 21969035) supplemented with 10% fetal bovine serum (FBS) (Gibco, A5256701) at 37°C and 5% CO_2. Human i3N iPSCs that harbor a doxycycline-inducible NGN2 transgene were a gift from Dr. Michael Ward (National Institutes of Health). iPSCs were cultured on Matrigel (VWR, 734-1440) in Essential 8 medium (ThermoFisher, A2858501). Methods for neuronal differentiation of i3N iPSCs were adapted from published protocols: iPSCs were plated on PLO (Sigma, P4638) in induction medium containing DMEM/F12 (Gibco, 11330032), 1× N2 supplement (Gibco, 17502048), 1× non-essential amino-acids (Gibco, 11140050), 200 mM L-glutamine (Gibco, 25030081), 10 μM Y-27632 dihydrochloride ROCK inhibitor (Selleck Chemicals, S1049) and 2 μg/ml doxycycline (Sigma Aldrich, D9891) to induce differentiation. At day 3 of differentiation, induction medium was replaced with i3Neuron medium containing Neurobasal (Gibco, 21103049) supplemented with 1× B-27 supplement serum free (Gibco, 17504044), 10 ng/ml

neurotrophin-3 (NT-3) (Thermo Fisher Scientific, PHC7036), 1 μg/ml mouse laminin (Gibco, 23017015) and 10 ng/ml BDNF (PeproTech, 450-02) to enable differentiation of NPCs to mature cortical-like neurons. Medium was replenished every 2-3 days.

METHOD DETAILS

Protein purification

Escherichia coli BL21 STAR (DE3) cells (ThermoFisher) were transformed with plasmid encoding the 6xHis-TDP-43 LCD construct (Addgene #98669) and expanded to a 2L volume. Protein expression was subsequently induced with 0.5 mM isopropyl-β-D-1-thiogalactopyranoside (Merck) for 4 h at 37°C and cells were collected by centrifugation. Bacteria were resuspended in lysis buffer (20 mM Tris pH 8.0, 500 mM NaCl, 1 mM DTT, EDTA-free protease inhibitor cocktail (Roche)), lysed by sonication on ice and centrifuged (40 min, 30.000g, 4°C) to pellet insoluble proteins. The pellet was resolubilized in denaturing buffer (20 mM Tris pH 8.0, 500 mM NaCl, 1 mM DTT, 8M urea) by sonication, followed by another round of centrifugation (40 min, 30.000g, 4°C). The re-solubilized proteins in the supernatant were collected, filtered (0.45 μm) and loaded onto an immobilized metal chelate affinity chromatography (IMAC) HisTrap™ HP column (Cytiva) using the Akta Püre system. After washing with denaturing buffer (20 mM Tris pH 8.0, 500 mM NaCl, 1 mM DTT, 8M urea, 10 mM imidazole), the 6xHis-TDP-43-LCD protein was eluted in the same buffer with a linear 10 mM to 500 mM imidazole gradient (Millipore) and further purified over a Superdex-200 16-600 size-exclusion column (Cytiva) in gel filtration buffer (20 mM MES pH 7.0, 8M urea). Finally, the fractions corresponding to the protein-of-interest were pooled and exchanged into storage buffer (20 mM MES, pH 5.5) by performing multiple dilution-concentration steps. The final protein sample was flash-frozen in liquid nitrogen and stored at -70°C at a concentration of 0.68 mg/ml (as determined by nanodrop). Each purification step was monitored by SDS-PAGE and Coomassie staining to visualize proteins.

Generation of recombinant TDP-43 LCD fibrils and seeds

Spontaneous fibril formation was performed by incubating recombinantly purified TDP-43 LCD protein (40 μM) in 20 mM MES (pH 5.5) at 25°C under shaking conditions (700 rpm; Provocell™) for a period of 7 days. For seeded fibrillization, sonicated TDP-43 LCD fibrils ("seeds") were added to monomeric TDP-43 LCD protein (40 μM, unless stated otherwise) at a 1:20 molar ratio and this reaction was incubated for 48 h at 25°C under shaking conditions (700 rpm). For each batch, quality of the newly generated fibrils was assessed by transmission electron microscopy (TEM). Fibril seeds were generated by sonicating recombinant TDP-43 LCD fibrils on ice using a probe sonicator (1 min, 50% amplitude) (Branson Digital Sonifier) and stored at -70°C. For aggregation assays in cells, seeds were sonicated a second time prior to transfection in U2OS cells using the bioruptor pico (Diagenode) for 15 min at a concentration of 10 μM, or prior to uptake in iPSC-neuronal cultures using a probe sonicator (1 min, 50% amplitude) at a concentration of 5 μM.

Transmission electron microscopy (TEM) of recombinant fibrils

To inspect morphology of TDP-43 fibrils and seeds by TEM, 6 μl of sample was spotted on a glow-discharged copper grid (01753-F, Ted Pella Inc.). The sample was adsorbed for 1 min, followed by three water washes and negative staining with uranyl acetate (2% w/v) for 30 s. Grids were examined using a JEM-1400 120 kV transmission electron microscope (JEOL) at an accelerating voltage of 80 kV. Quantifications of seed length, fibril width, fibril twist and helical crossover length were performed manually using ImageJ.

Congo red staining of recombinant fibrils

Droplets (5 μL) of TDP43 LCD amyloid fibrils were deposited on glass slides and permitted to dry slowly in ambient conditions in order to form thin films. The films were stained with a Congo red (Sigma) solution (5 μl of 0.1% w/v) prepared in milli-Q water for 10 min. Washing was performed with milli-Q. Glass slides were further imaged using a brightfield microscope (ZEISS) with polarization filter.

Fourier-transform infrared spectroscopy (FTIR)

30 μL of TDP43 LCD fibril solution was loaded onto and analyzed using an Invenio FT-IR spectrometer equipped with BioATRCell II (Bruker). FT-IR spectra were recorded as averages of 256 spectral scans at 2 nm^{-1} resolution in transmission mode to improve signal-to-noise ratio. Background correction was performed by subtracting spectrum obtained from the matching buffer (MES pH 5.5) using the OPUS software (v8.5.29).

Thioflavin-T (ThT) kinetic assays

Different concentrations of soluble TDP-43 LCD in 20 mM MES (pH 5.5) were incubated in black 384-well microplates (Greiner) and supplemented with 25 μM ThT (T3516, Merck). ThT binding was measured over time at 25°C in a FluoStar Omega plate reader (BMG Labtech) by excitation at 440 nm and emission at 480 nm. To assess the effect of seeding on aggregation kinetics, TDP-43 LCD monomers were supplemented with seeds (5%) and ThT measurements were performed as described above. For each experiment, every condition was tested in triplicates.

Seeding assay in cultured cell lines

Seeding assays were performed in genetically engineered U2OS cells that overexpress TDP-43^{mNLS}-Clover under a doxycycline-inducible promotor[11] or wild-type U2OS cells. For seeding assays, cells were cultured in 96-well plates (PhenoPlate, PerkinElmer)

(8000 cells/well), glass-bottom 8-well chamber slides (Ibidi) (30,000 cells/well) or 6-well plates (250,000 cells/well). When investigating the aggregation of TDP-43^{mNLS}-Clover, expression was induced by supplementing the culture medium with doxycycline (1 μg/ml) (D9891, Sigma-Aldrich) for the duration of the experiment (unless mentioned otherwise). No doxycycline was added for experiments in which endogenous TDP-43 aggregation was monitored. After 24 h, sonicated TDP-43 LCD fibrils were introduced into cultured cells using Lipofectamine-3000 (Invitrogen) according to the manufacturer's guidelines. For dose-response seeding experiments, 10 different final concentrations of TDP-43 LCD seeds were tested, ranging from 0 nM to 250 nM. For other experiments, final seed concentrations of 50 nM and 100 nM were used when assessing aggregation of TDP-43^{mNLS} and TDP-43^{WT}, respectively. For "ageing" experiments in which cells with aggregates were cultured for extended periods, cell proliferation was suppressed using reduced culture medium (containing 1% FBS) supplemented with cell-cycle inhibitor Palbociclib (1 μM, ApexBio). To evaluate seeded aggregation of transiently expressed TDP-43-Clover, 100 nM TDP-43 LCD seeds and/or 25-50 ng TDP-43-Clover plasmids were simultaneously transfected in U2OS cells using Lipofectamine-3000, after which cells were incubated for 24 h.

Seed transfection experiment with bortezomib/MG-132 treatment

Reporter U2OS cells were cultured in 6-well plates in the presence of doxycycline (1 μg/ml) (D9891, Sigma-Aldrich) to induce expression of TDP-43^{mNLS}-Clover and, 24 h later, transfected with TDP-43 LCD seeds (50 nM) using Lipofectamine-3000 reagent (Invitrogen). Following a 6-h incubation period with the seed transfection mix, cells were trypsinized and re-plated in a 96-well plate (PhenoPlate, PerkinElmer) at 8,000 cells/well. By performing "bulk" seed transfection before transferring cells to 96-well plates, we ensure that the number of seeded cells at the start of the experiment is similar in every well. 24 h after seed transfection, medium was exchanged to reduced culture medium (1% FBS) supplemented with 4 nM Bortezomib (Sigma Aldrich) or 40 nM MG-132 (Sigma Aldrich), or 1 μM Palbociclib (ApexBio) in control conditions. The same batch of bortezomib was used for all experiments, due to observed batch-to-batch variability with respect to the concentration at which the reported effects on U2OS cells were observed. In each experiment, treatments were performed in duplicates or triplicates. Medium change with fresh compounds was performed every 2 days. Doxycycline (1 μg/ml) was added to the culture medium at every step to ensure continuous TDP-43-Clover expression.

Human iPSC culture, neuronal differentiation and seeding assay

Human iPSCs expressing doxycycline-inducible neurogenin-2 (NGN2)[58,74] were cultured on Matrigel-coated dishes in Essential 8 Flex (E8 flex) medium (Gibco, A2858501). To generate the stable TDP-43^{WT}-Clover iPSC line, iPSCs were transduced with a lentivirus expressing C-terminally Clover-tagged human wild-type TDP-43. Differentiation of iPSCs to i3Neurons was performed as previously described[58,74] with minor modifications: to avoid loss of aggregate-containing cells in response to seed treatment, iPSCs were directly plated at day 0 on PLO-coated 8-well Ibidi slides / 12-well plates in induction medium containing DMEM/F12 (Gibco, 11330032), 1× N2 supplement (Gibco, 17502048), 1× non-essential amino acids (Gibco, 11140050), 200 mM L-glutamine (Gibco, 25030081), 10 μM Y-27632 dihydrochloride ROCK inhibitor (Selleck Chemicals, S1049) and 2 μg/ml doxycycline (Sigma Aldrich, D9891) to induce differentiation. After 24 h, fresh induction medium supplemented with doxycycline was mixed with sonicated TDP-43 LCD seeds (at a final concentration of 250 nM) and added to differentiating neuronal progenitor cells (NPC) for 2 days to allow uptake. At day 3 of differentiation, induction medium was replaced with i3Neuron medium containing Neurobasal (Gibco, 21103049) supplemented with 1× B-27 supplement serum free (Gibco, 17504044), 10 ng/ml neurotrophin-3 (NT-3) (Thermo Fisher Scientific, PHC7036), 1 μg/ml mouse laminin (Gibco, 23017015) and 10 ng/ml BDNF (PeproTech, 450-02) to enable differentiation of NPCs to mature cortical-like neurons. Media was replenished every 2-3 days.

Immunocytochemistry

Cells were fixed with 4% PFA in PBS for 15 min at room temperature (RT) at the indicated timepoint. After three PBS washes, cells were permeabilized and blocked with blocking solution (U2OS cells: 0.3% Triton, 3% BSA, 5% normal serum in PBS; iPSC-neurons: 3% normal donkey serum, 0.25% Tween-20 in PBS) for 1 h at RT. Cells were then incubated overnight at 4°C with primary antibody in antibody diluent (U2OS cells: 0.3% Triton, 3% BSA in PBS; iPSC-neurons: 3% normal donkey serum, 0.25% Tween-20 in PBS). Following primary antibody dilutions were used:

Antibodies	Source	Identifier	Dilution
TDP-43	ProteinTech	10782-2-AP	1/500
Phospho-TDP-43	BioLegend	829901	1/500
FUS	Bethyl Laboratories	A300-302A	1/500
hnRNPA2/B1	Santa Cruz	sc-374053	1/500
Polyhistidine	Sigma Aldrich	H1029	1/500
Ubiquitin	Santa Cruz	sc-8017	1/500
p62	Progen	GP62-C	1/500

(*Continued on next page*)

Continued

Antibodies	Source	Identifier	Dilution
PSMA1	Invitrogen	PA1-963	1/500
PSMC4	Arigo Biolaboratories	ARG43994	1/100
LAMP1	DSHB	H4A3	2.5 μg/ml
EEA1	Sigma Aldrich	E4156	1/200
Neurofilament H	Merck	AB5539	1/500
Stathmin-2	Proteintech	67204-1-Ig	1/200
Tau	Invitrogen	MN1000	1/500
NeuN	Genetex	GTX133127	1/200
MAP2	Novus Bio	NB300-213	1/1000

After ON incubation with primary antibody, the sample was washed three times with PBS. Next, cells were incubated with Alexa488-, Cy3- or Alexa647-labelled secondary antibodies (Jackson ImmunoResearch) at 1/500 in antibody diluent for 1 h at RT. Three additional PBS washes were performed and cells were incubated with DAPI (1 μg/ml in PBS; Merck) for 15 min at RT. After a final PBS wash, samples were preserved in PBS at 4°C.

Imaging and quantification of TDP-43 aggregation/mislocalization

Image acquisition for quantification of seeded aggregation in U2OS cells was performed in 96-well plates (Phenoplate, PerkinElmer) by high-content imaging using the Operetta CLS (PerkinElmer). For each well, 17-21 images were acquired as Z-stacks using a 20X (NA 1.0) or 40X (NA 1.1) water-immersion objective. Confocal image acquisition was performed using a Nikon TiE A1R laser-scanning confocal microscope equipped with an HD resonant scanner. The system utilized a 403 nm (diode, 130 mW), 488 nm (diode, 50 mW), 561 nm (diode, 50 mW), and 640 nm (red diode, 100 mW) lasers. Emission filters were configured for blue (425-475 nm), green (500-550 nm), and red (570-616 nm) spectral ranges. High-magnification images were acquired using an Apo 60x λS DIC N2 oil immersion objective (NA 1.4). Image acquisition for assessment of seeded aggregation in iPSC-neurons was performed in glass-bottom 8-well chamber slides (80827, Ibidi) using high-content imaging with the Operetta CLS. For each well, 45-60 images were acquired as Z-stacks using a 40X (NA 1.1) water-immersion objective. High-magnification images were acquired using the previously described Nikon TiE A1R.

Time-lapse fluorescence imaging

Time-lapse imaging to monitor TDP-43-Clover mislocalization and aggregation in response to seeding was performed on the Operetta CLS using a 40X (NA 1.1) water immersion objective with temperature and CO_2 control. In each well, 15 images were acquired as Z-stacks with 1-h intervals for a period of 48 h, starting immediately after seed transfection. Data were processed using Harmony software. In order to monitor degradation of TDP-43-Clover aggregates and cell viability over time, time-lapse microscopy was performed on the Nikon A1R TiE confocal microscope with a 40X objective at 37°C with CO_2 control (Okolab) using a motorized XYZ stage with focus drift correction (Nikon Perfect Focus System). In each well, 10-20 regions-of-interest were manually selected and imaged as Z-stacks with 1-h intervals for a total duration of 48 h. Data were processed using NIS Elements Advanced Research software. Analysis was performed by manually tracking individual cells to assess degradation of TDP-43 aggregates and cell death. Cells were only included for quantification if they (1) were present in the imaging field at the start of the experiment and (2) stayed within field-of-view throughout the entire 48 h period, or underwent cell death within this time window. Prior to each time-lapse experiment, U2OS cells were labelled with CellTracker Deep Red dye (C34565, Invitrogen) or Cell Tracking Red dye (ab269446, Abcam) and cultured in FluoroBrite™ DMEM (A1896701, Gibco) supplemented with FBS (Gibco, A5256701). iPSC-neuron precursors were cultured in standard induction medium. 5-day old iPSC-neurons were cultured in i3Neuron medium with modified neurobasal without phenol red (Gibco, 12348017).

Fluorescence recovery after photobleaching (FRAP)

For FRAP experiments, TDP-43-Clover expressing U2OS cells or iPSC-neurons were cultured on Ibidi chamber slides (80807) in FluoroBrite™ culture medium (Gibco) or modified i3Neuron without phenol red (Gibco, 12348017), respectively. FRAP measurements were performed on a Nikon A1R TiE microscope equipped with an APO 60x/1.4 oil objective using the NIS Elements software. The microscope stage was temperature and CO_2 controlled (37°C, 5% CO_2). For photobleaching, we defined a circular region-of-interest (ROI) that was excited using a 488 nm diode laser at 100% power. Clover fluorescence recovery after bleaching was monitored for 3 min at intervals of 2 s (16x), followed by 10 s intervals (15x). For each condition, at least 10 TDP-43-Clover aggregates/condensates were measured from 3 independent experiments.

Fluorescence lifetime imaging microscopy (FLIM)

To probe the microenvironment of Clover[75] in different TDP-43 condensation/aggregation phases, U2OS cells expressing TDP-43-Clover were grown in glass-bottom well-chambers (Ibidi, 80827) or microscopy-ready polymer-bottom 96 well-plates (Phenoplate, PerkinElmer). Transfection with seeds was done as described above and for two timepoints, 1 and 8 days. FLIM was performed with a

confocal microscope (LSM 880, Carl Zeiss, Jena, Germany) using a 63x water immersion objective (C-ApoChromat 63x/1.20 W Korr M27, *Carl Zeiss*) and detection with a photomultiplier tube (Zeiss BiG-2 GaAsP detector) where a window of detected wavelengths was selected (FF01-525/50-25, Brightline, Semrock). Excitation was done with the use of a Diode 488 nm pulsed laser (Becker & Hickl), suitable for fluorescence lifetime imaging, set at a repetition rate of 50 MHz and photon timing processed with a time correlated single photon counting card (Multiharp 150N, PicoQuant, Berlin, Germany). To avoid changes in the instrument response function, laser percentage was kept constant while laser power was adjusted by physically clipping part of the laser beam before coupling it into the optical fiber entering the scan head. Laser powers were such that the highest pixel count rate was below 10% of the laser repetition rate. Confocal intensity images and FLIM images were recorded simultaneously via Zen Black 2.3 SP1 (Carl Zeiss) and Symphotime software (PicoQuant), respectively.

Immunoblotting

Cells were lysed in RIPA Lysis and Extraction buffer (ThermoFisher) supplemented with a protease inhibitor cocktail (ThermoFisher) and centrifuged at 13,000 g for 20 min at 4°C to collect the supernatant. For immunoblotting, the samples were quantified using the bicinchoninic acid (BCA) kit (ThermoFisher) and boiled in Laemmli sample buffer for 5 min at 98°C. Proteins were separated in 10% Mini-PROTEAN® TGX™ gels (Bio-Rad) and blotted onto PVDF membranes. Membranes were blocked using 5% non-fat dry milk for 1 h and probed with primary antibodies anti-TDP-43 (Proteintech #10782-2-AP, 1:2000) and anti-vinculin (Sigma #V9131, 1:10,000) overnight at 4°C, followed by horseradish peroxidase-conjugated secondary antibodies (1:5000, Jackson ImmunoResearch) in TBS blocking buffer with 0.1% Tween20 for 1 h at RT. Blots were imaged with Pico enhanced chemiluminescence (ECL) reagent (Pierce) using the iBright scanner (ThermoFisher). Quantification of bands intensity was performed using ImageJ (NIH).

RT-PCR for cryptic transcripts

TDP-43^{mNLS}-Clover expressing U2OS cells or naive U2OS cells were cultured in 6-well plates and transfected with TDP-43 LCD fibril seeds (50 nM or 100 nM, respectively) or control transfection mix as described above. Cells were collected 48 h after transfection. For seeding in i3Neurons, neural progenitor cells (1 day post-induction) were directly treated with 250 nM fibril seeds or control buffer in 24-well plates, and collected 5 days later as iPSC-neurons. Total RNA was extracted using TRIzol™ reagent (Invitrogen, 15596026) according to the manufacturer's guidelines. The purified RNA was subjected to DNAse treatment (Invitrogen, 18068015) and its concentration measured by nanodrop. For cDNA synthesis, 1 μg of total RNA was reverse transcribed using the high-capacity reverse transcription kit (Applied Biosystems, 4368814) according to the instructions of the manufacturer. RT-PCR reactions were performed with 50 ng cDNA using Q5 High-Fidelity DNA polymerase (NEB, M0491), with the following cycling parameters:

Initial denaturation: 98°C for 30 s; 40 cycles: 98°C for 10 s, 60°C/64°C/68°C for 30 s (depending on primer pair), 72°C for 20 s; Final extension: 72°C for 5 min.

For splicing analysis, RT-PCR products were separated on a 2% agarose gel. Primers are listed in the key resources table.

Image-based FACS

TDP-43^{mNLS}-Clover expressing U2OS cells were transfected with buffer control or seed (50 nM) mix in T-75 flasks and collected 48 h later for FACS. Both seed and control transfections were performed in triplicates. For each sample, cells were isolated using a 5-laser BD FACSDiscover S8 with BD CellView Technology, using a 100 micron nozzle at 20 psi. Populations of interest were identified based on both fluorescent and imaging parameters and subsequently sorted using the purity mask with BD FACSChorus v5.1 Software. Cells with aggregates were sorted from "aggregated population" in seed-transfected samples. Cells without aggregates were sorted from control samples. For each sample/condition, 70,000 cells were collected for downstream RNA sequencing.

RNA sequencing

RNA was extracted from FACS-sorted U2OS cells with TDP-43^{mNLS}-Clover aggregates or FACS-sorted U2OS cells with diffuse TDP-43^{mNLS}-Clover (control) from 3 independent seeding experiments using the innuprep RNA minikit 2.0. Sequencing of RNA samples was performed on Element AVITI system (2x150 base pair, paired end). RNA-Seq processing and analyses were performed as described below.

QUANTIFICATION AND STATISTICAL ANALYSIS

Image analysis for quantifications of TDP-43 aggregation

Automated analysis to determine number and size of TDP-43 inclusions in U2OS cells was performed using Harmony analysis software (Perkin Elmer). Fibril-induced inclusions were identified based on anti-TDP-43 and/or TDP-43-Clover signal, in combination with phospho-TDP-43 signal. Quantification of nuclear TDP-43 levels was performed using ImageJ by manually segmenting the nucleus area and measuring anti-TDP-43 mean fluorescence intensity at the Z-plane corresponding to the center of the nucleus. Analysis of TDP-43 aggregate morphology was performed manually using Harmony. Aggregates with a dense core at their center were classified as "compacted." Aggregates that present as a connected network of filaments, in the absence of a fibril core, were defined as "filamentous." Aggregates consisting of individual fragments, either shaped as granules or filaments that are no longer interconnected, were classified as "fragmented." For analysis of TDP-43 aggregation in iPSC-neurons, the number of cells with cytoplasmic

aggregates, different aggregate morphologies, nuclear depletion, and increased risk of cell death were quantified manually using Harmony for image visualization. For stathmin-2 quantification, fluorescence intensity from unsaturated images captured with identical confocal settings was quantified manually using ImageJ (NIH).

Fluorescence recovery after photobleaching (FRAP) analysis

FRAP data were analyzed using ImageJ as described previously.[76] Shortly, the mean fluorescence intensity of the bleached object at each timepoint was normalized to the intensity prior to bleaching ($F_{pre\text{-}bleach} = 1$), while the intensity measured immediately after photobleaching (at t = 0) was set to zero ($F_{t=0} = 0$). In addition, fluorescence intensity of an unbleached object in the field-of-view was measured over time as internal reference, and used to normalize the FRAP curve of the bleached object to control for unwanted acquisition photobleaching. Fluorescence recovery was plotted using GraphPad Prism and fitted with a one-phase exponential curve to extract the recovery half-time ($t_{1/2}$).

Fluorescence lifetime imaging (FLIM) analysis

FLIM analysis was performed with the phasor module of an open-source software (PIE Analysis with MATLAB).[77] Firstly, phasor lifetime of the fluorescent protein in the different TDP-43 maturity conditions was processed against a previously recorded measurement of ATTO 488, which has a known fluorescence lifetime of 4.1 ns. Afterwards, pixels, where a minimum of 150 photons were collected,[43] were analyzed by manually selecting ROIs, corresponding to previously established dilute, dense, and aggregated states. Lifetime values found at the center of mass of the corresponding phasor plots were used for statistical analysis. Images were false-colored with a color gradient corresponding to determined fluorescence lifetime values.

Quantification of LAMP1-TDP-43 Spatial Distribution

Image analysis was performed using a custom ImageJ macro script in FIJI (version 1.54f) with the MorphoLibJ plugin (version 1.6.3). Image datasets were denoised using the Denoise.ai tool in NIS-Elements software, version 6.02.01. Individual cellular regions of interest were initially delineated through manual annotation of maximum intensity Z-projections. Cell boundaries were determined based on signals observed in LAMP1 and DAPI channels. These manual annotations were subsequently utilized as reference masks for automated cell segmentation, wherein the LAMP1 channel was processed using Gaussian blurring ($\sigma = 10$) followed by MinError thresholding. Nuclear segmentation was achieved by applying a Gaussian blur ($\sigma = 3$) to the DAPI channel followed by Default algorithm thresholding. To separate touching nuclei, a 3D watershed transformation was applied, and objects smaller than 1000 μm^3 were removed to exclude debris and partial nuclei at image boundaries. Cytoplasmic regions were defined by subtracting the nuclear masks from the cell masks.

LAMP1-positive vesicles were detected using a difference of Gaussian approach ($\sigma_1 = 2$ pixels, $\sigma_2 = 10$ pixels) implemented with GPU acceleration via CLIJ2. These parameters were optimized for the expected size of LAMP1-positive vesicles. TDP-43 clusters were identified through sequential application of a median filter (radius = 5 pixels), background subtraction (rolling ball radius = 50 pixels), and intensity thresholding at 7000 intensity units.

For the spatial analysis, we measured the nearest distances in 3D between LAMP1-positive vesicles and TDP-43 clusters in 3D using calibrated voxel dimensions. To account for cell size heterogeneity, distances within each cell were normalized by dividing by the maximum distance within that cell's cytoplasmic volume. The resulting normalized distances were binned (bin size = 0.1) and expressed as fractions of total cell volume.

RNA-seq processing, differential gene expression and splicing analysis

Raw, paired FASTQ files were first filtered using fastp v0.23.2 (https://doi.org/10.1002/imt2.107), these filtered FASTQ files were then mapped to, and quantified against the hg38 genome using STAR v.2.7.11a (https://doi.org/10.1093/bioinformatics/bts635). Gene counts per sample were combined and differential gene expression analysis was performed using pydeseq2 v0.4.10 (https://doi.org/10.1093/bioinformatics/btad547), with Condition used as the comparison attribute. A principal component analysis was performed using sklearn v1.5.1 (https://www.jmlr.org/papers/v12/pedregosa11a.html). For splicing analysis, all junctions were identified per sample using regtools v1.0.0 (https://doi.org/10.1038/s41467-023-37266-6) with the junctions command the following arguments: -a 6 -m 30 -M 500000 -s RF. Following junction identification, junctions were quantified using the leafcutter_cluster_regtools.py script from leafcutter commit ID: 2c9907e (https://doi.org/10.1093/bioinformatics/btaa259). Identified junctions were annotated based on known gene CDSs overlapping the junction in a strand aware manner using BEDtools v2.31.1 (https://doi.org/10.1093/bioinformatics/btq033). Differential junction expression analysis in an identical manner as described above, with the exception that the independent filtering feature was disabled. KEGG pathway analysis was performed using STRING software (https://string-db.org) on differentially upregulated genes in "cells with aggregates" (log2foldchange > 0.6 and p adj. < 10^{-40}).

Statistical analysis

Statistical analysis was performed using GraphPad Prism as indicated in figure legends. To compare means of 2 datasets, unpaired Student's t test was used. To compare more than 2 datasets, we used one-way analysis of variance test (ANOVA) followed by a post hoc Tukey test, or a post hoc Dunnett's test in case each group was compared with a single control group. All graphs display replicates as individual data points (as defined in figure legend) with mean ± standard deviation (SD). Significance threshold was defined at 0.05. Significance levels are indicated as follows: ****p < 0.0001, ***p < 0.001, **p < 0.01, *p < 0.05, ns, non-significant.